

Coherent Combining and Long Coherent Integration for BOC Signal Acquisition under Strong Interference

Chun Yang¹ | Andrey Soloviev¹ | Ananth Vadlamani¹ | Joung C. Ha²

¹ QuNav, LLC, Ft. Walton Beach, FL, USA

² Air Force Research Laboratory
WPAFB, OH, USA

Correspondence

Chun Yang, QuNav, LLC
2 Park Circle SE, Unit B
Ft. Walton Beach, FL 32548, USA
Email: yang@qunav.com
+1 650-430-6267

Abstract

A coherent combining and long coherent integration (CCLCI) scheme is presented for standalone direct acquisition of binary offset carrier (BOC) signals under strong radio frequency interference (RFI). To mitigate the ambiguity of BOC signals, a split-spectrum method extracts the upper and lower sidebands of a BOC signal, treats them separately as two binary phase shift keying (BPSK) signals, and finally combines the results to recover the loss due to splitting. The CCLCI scheme burns through strong interference by building up the desired weak signal while averaging out noise and interference. It exploits all information available (L1 and L2, upper and lower sidebands, odd and even chips, and I- and Q-components) by applying coherent combining across signal components and long coherent integration over time, followed by noncoherent accumulation if necessary. Issues and enabling techniques are described. The results of an embedded implementation in demonstration with a GPS RF simulator are analyzed.

Keywords

coherent combining, coherent integration, direct acquisition, split-spectrum signals, weak signals

1 | INTRODUCTION

Binary offset carrier (BOC) modulation was initially developed for GPS modernization, leading to the new military M-code BOC(10,5) at L1 and L2 (Barker et al., 2000; Betz, 1999). It was quickly adopted by other GNSS constellations and is now used in L1C_D BOC(1,1), L1C_P TMBOC(6,1,1/11), E1_A BOC(15,2.5), E1_B/E1_C CBOC(6,1,1/11), E6_A BOC(10,5), E5 AltBOC(15,10), and B1A BOC(14,2), B1C_D BOC(1,1), B1C_P QMBOC(6,1,4/33), B2a and B2b AltBOC(15,10), and B3A BOC(15,2.5), among others. The split-spectrum offered by BOC modulation was originally sought for its easy sharing of the crowded spectrum with the legacy binary phase shift keying (BPSK) signals that occupy the respective band centers. It turns out that the split-spectrum possesses a larger Gabor bandwidth, producing better ranging performance in terms of accuracy and multipath (Betz, 2015; Pany, 2010).

The acquisition and tracking of a general BOC signal encounter the issue of multiple peak ambiguity (Gusi et al., 2016) even though it is less of a problem for multiplexed BOC (MBOC) signals due to low subcarrier rate (Pany, 2020). Many

methods have been proposed to address this problem by: a) avoiding the ambiguity (Fine and Wilson, 1999; Heiries et al., 2004); b) making it BPSK-like (Burian et al., 2006); c) suppressing side peaks in a new unambiguous function obtained with a combination or modulation of local BOC reference codes (Julien et al., 2007; Ward, 2003a); and d) correlating the incoming BOC signal with a local auxiliary reference code to produce a single narrow peak (Hao et al., 2020; Yao, 2012).

Most of these methods, though, are designed for BOC signal tracking (Hodgart & Simons, 2012; O'Driscoll & Curran, 2016). For the initial signal acquisition, however, one simple method (similar to a) and b) above) to avoid the ambiguity is to extract the split spectra, treat them separately as two BPSK signals, and then combine the results at the end. There are several benefits to this approach. First, when the spectra are extracted from the band edges, it avoids the band center where interference is likely to concentrate. Second, for each extracted split-spectrum (a sideband), the bandwidth is reduced by half as is the sampling rate. The processing throughput of each sideband is thus reduced even though the total loading remains the same. Third, the correlation peak for a sideband is wider, the spacing between search grid points is larger, and the number of search points covering the same uncertainty interval is thus smaller, leading to faster acquisition in average. However, to recover the reduced strength of each sideband signal, the individual correlations have to be combined.

Coherent combining across signal components and coherent integration over time are techniques of high-sensitivity GNSS receivers (Dovis & Ta, 2012; Kong, 2017; Seco-Granados et al., 2012) used to achieve better signal detection, tracking, and measurement. Coherent combining of multiple signals may involve the upper and lower sidebands of a BOC signal (Yang et al., 2020a) and signals on different bands (Deambrogio et al., 2013; Yang & Soloviev, 2016). Depending on their separation, the signal components are subject to different uncertainties in signal propagation and group delay, antenna/analog electronics impairments, and frequency and phase offsets, which require due compensations for the method to be effective.

On the other hand, coherent integration over time needs to face large initial frequency (and associated code chipping rate) errors especially during high dynamics (Wu et al. 2015) and sign reversals of data bits and secondary codes (Borio, 2008; Leclère et al., 2017; Svaton & Vejražka, 2020). Moreover, during long integration, clock instability becomes critical (Serna et al., 2010). In addition to classical coherent and non-coherent integration and combination thereof, a variety of semi-coherent and differentially coherent (Borio et al., 2009; Gómez-Casco et al., 2020; Esteves et al., 2016), as well as generalized detection (Corazza & Pedone, 2007) schemes are available. Notable is the comparative performance evaluation of such techniques in indoor, urban, and space environments (Dominguez et al., 2016) wherein the effects of oscillators such as temperature-compensated crystal oscillators (TCXOs), oven-controlled crystal oscillators (OCXOs), and chip-scale atomic clocks (CSACs), as well as the near-far problem caused by severe attenuation of direct signals and strong cross-correlations between codes are studied.

Non-coherent integration including the semi, differential, and generalized coherent variants (Dovis & Ta, 2012; Esteves et al., 2016; Gómez-Casco et al., 2020; Kong, 2017) applies a nonlinear operation (delay-conjugate-multiply) so as to remove data bits and residual Doppler shift. As such, it suffers from an instantaneous signal-to-noise ratio (SNR) degradation due to the squaring loss (Lowe, 1999; Strassle et al., 2007) as the price paid for the benefit of subsequent longer power accumulation.

However, most non-coherent integration implementations do not consider code phase migration, which may exceed one code chip in a long run, and the schemes themselves do not produce a refined estimate of frequency (or phase or data bit)

that is necessary to close tracking loops. Besides, a hybrid implementation that adds up different detectors and sums over multiple delays is computationally demanding (Yang et al., 2020a). For these reasons, we focus on *coherent combining and long coherent integration* (CCLCI) in this paper.

Coherent combining is more gainful than the non-coherent counterpart particularly when the incoming signal is weak and/or when an interference signal is present. Long coherent integration requires a rather fine frequency search grid (Pany et al., 2010; Soloviev & Dickman, 2011; Soloviev et al., 2012; Yang & Han, 2006; Yang & Soloviev, 2016), which would be prohibitive if the fine frequency search grid were implemented by brute force. Alternatively, appropriate short correlations can be performed, followed by post-correlation phase alignment and integration. In addition to dealing with unknown navigation data bits that change sign over the long integration interval, phase alignment is required to compensate for code migration and frequency divergence, which are two detrimental effects unique to split-spectrum signals when integrated over a long period of time.

This paper presents a particular implementation of coherent combining and long coherent integration (CCLCI), which: a) refines frequency search resolution in stages; b) compensates for code phase migration; c) compensates for frequency divergence when combining upper and lower sidebands; d) rectifies data bit signs when needed; and e) makes delay, frequency, and phase adjustments when combining multiband sidebands.

The staged accumulation reduces the computation loading by applying coarse search at a high data rate and fine search at a low data rate. Note that the upper and lower sidebands of a BOC signal are complex conjugates of each other, and the Doppler frequency shift experienced by each sideband is slightly different. Such a difference becomes significant when the frequency divergence between the upper and lower sidebands becomes comparable to the frequency resolution required for the long coherent integration, which needs to be compensated for prior to coherent combining.

In this paper, the CCLCI method for standalone direct acquisition of multi-band split-spectrum BOC signals is described and demonstrated. It is based on the work of Yang et al. (2019), who introduced the basic concept with initial simulation results, and Yang et al. (2020b), who presented embedded implementation results. As a continuation, this paper presents three new results, namely: a) comparison of different combinations of coherent/non-coherent integration schemes; b) evaluation in terms of a classical metric of *receiver operating characteristics* (ROC); and c) discussion of issues related to clock stability for handover from acquisition to tracking.

The system concept and architecture are first reviewed. Key issues and enabling techniques are then described. The CCLCI scheme is implemented on a *software-defined receiver* (SDR) platform consisting of a field programmable gate array (FPGA) and an advanced RISC machine (ARM) processor. Embedded implementation of CCLCI up to one second and demonstrations with radio-frequency (RF) signals generated by a Spirent GPS RF Simulator are presented to illustrate the functionality and performance. Results of the embedded demonstrations are analyzed together with comparisons and trade-offs between *coherent integration* (CI) and various combined coherent integration and *non-coherent integration* (CI/NCI) schemes. The paper is concluded with a summary and future work.

2 | CONCEPT AND ARCHITECTURE

GPS signal acquisition consists of dividing the *initial time uncertainty* (ITU) and *initial frequency uncertainty* (IFU) zones into a grid of search points and then testing the search points in a certain order until the signal is detected at one search point

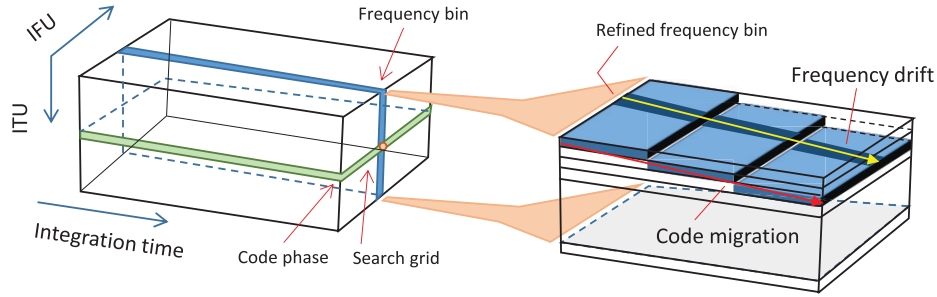


FIGURE 1 Code migration and frequency drift (right) within a search cube of code phase \times frequency bin \times integration time (left)

or not. Each test consists of correlating the incoming signal samples with those of a local replica generated using the time-frequency parameters at the test point.

When the incoming signal is extremely weak due to dense foliage or when an interference signal is present, the use of CCLCI can boost signal strength while averaging out the noise and/or interference signals. The ITU and IFU zones are divided into code phases and frequency bins. At each pair of code phase and frequency bin (a test point of the search grid) the signal is accumulated over a long integration time, forming a cube of *code phase \times frequency bin \times integration time* as shown in Figure 1.

Each frequency bin is fanned out for a refined frequency search required to enable long integration as shown in Figure 1. In terms of refined frequency bins, frequency spreads due to acceleration, clock drift, and frequency divergence between upper and lower sidebands (and different frequencies) become significant, which require proper frequency alignment.

Similarly, code phase is subject to migration with random variations. The excursions in and out of code phases and/or frequency bins reduce the effectiveness of coherent integration. The dwell of the signal around a test point determines the maximum coherent integration interval, beyond which non-coherent integration is needed with due code and frequency alignments.

An example of standalone direct acquisition of split-spectrum signals is the state-of-the-art design DirAc based on massive parallel matched filters (Betz et al., 2004, 2008; Fishman & Betz, 2000). The CCLCI method of this paper differs from DirAc in that it is not only scalable in correlator parallelism for code phase and Doppler frequency search (breadth) but also scalable in integration interval (depth). In our design, there is no architectural limitation to the number of parallel correlators. More importantly, the parallel correlators can operate on endless samples (subject to the effective dwell limitation).

An implementation of CCLCI with massive parallel correlations is shown in Figure 2, which has six major components (Yang et al, 2019, 2020b):

- **Dual-frequency antenna and RF front-end:** A dual-frequency antenna is connected to a dual-frequency RF front-end (analog) in which the signals received at L1 and L2 are amplified, band-pass filtered, and down-converted to a suitable intermediate frequency (IF) before complex-sampling at tens of mega samples per second or msp/s (digital).
- **Time-frequency uncertainty zone divided into search tiles:** The time-frequency uncertainty zone is divided into search tiles with each search tile containing a number of search points that can be covered simultaneously by the hardware correlators in parallel. The spacing between two search points in

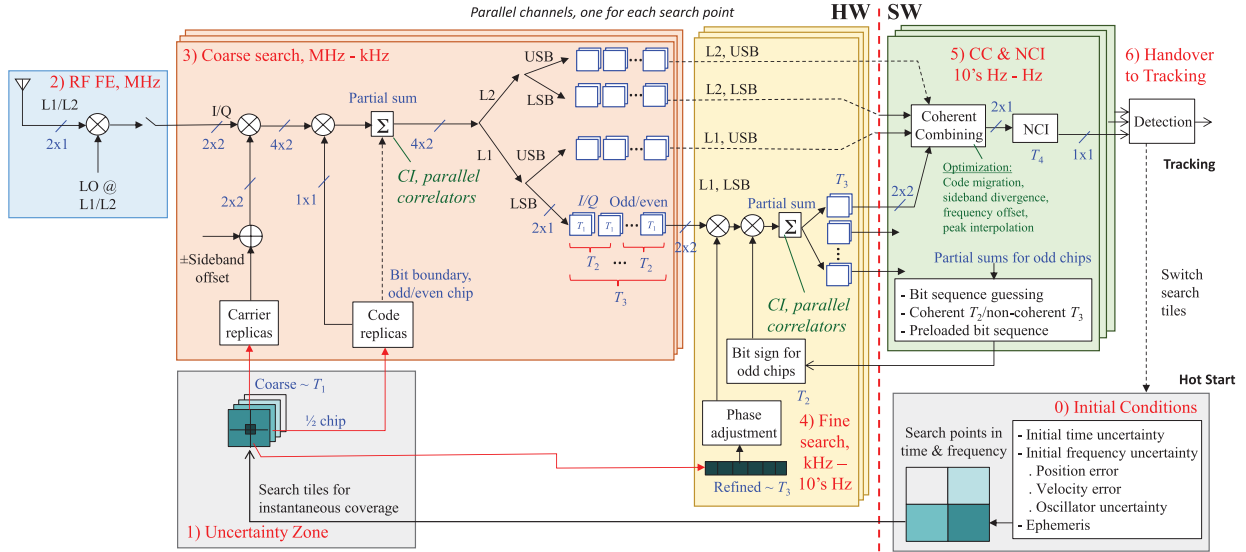


FIGURE 2 Standalone direct acquisition of BOC signals with massive parallel correlators in the CCLCI scheme

time is $\frac{1}{2}$ chips while the spacing in frequency is $1/(2T_1)$. When $T_1 = 1$ ms, the frequency spacing is 500 Hz.

- Coarse-search in time and frequency:** For each frequency L1 or L2, the upper and lower sideband signals are extracted, using the known frequency offsets from the frequency bin under search, for parallel processing into four complex partial sums L1-upper sideband (USB), L1-lower sideband (LSB), L2-USB, and L2-LSB, respectively.
- Fine-search in frequency:** The partial sums of T_1 are subject to a frequency error as large as $1/(2T_1)$ Hz. For coherent integration to T_3 , the tolerable frequency error cannot be larger than $1/(2T_3)$ Hz. As a result, a secondary frequency search is conducted with a refined frequency resolution of $1/(2T_3)$ Hz. The partial sums of T_1 are first phase-rotated and then accumulated up to T_2 (a data bit) and then to T_3 . The partial sums per data bit (T_2) can then be processed in different ways depending on the knowledge of the bit sequence to be discussed later.
- Coherent combining, coherent integration, and non-coherent integration:** For each T_3 (the coherent integration interval), the eight complex partial sums, namely, the data and data-less components of the upper and lower sidebands on L1 and L2, are first added coherently. If T_3 is large, however, the coherent integration needs to account for the following aspects for best results.
 - *Code migration:* Associated with each search frequency, there is a maximum frequency error of $\frac{1}{2}$ frequency bin, which translates to a corresponding code Doppler. As a result, the signal may not dwell on a single search code phase but rather over the adjacent few if the integration time is longer than what takes the code to migrate across a spacing of $\frac{1}{2}$ chips. To achieve a larger gain, the signal accumulations in the adjacent code phases are aligned and summed up.
 - *Sideband divergence:* The undulation of correlation due to code migration introduces an amplitude modulation to both the upper and lower sideband signals. Since the upper and lower sideband signals are complex conjugates

to each other, their respective correlation peaks are shifted in opposite directions in frequency, as is the Doppler shift, leading to the so-called sideband divergence. If the refined frequency search bin is smaller than the total shift in frequency, an alignment in frequency is needed before summing up the two sidebands.

- *Inter-frequency delay offset*: Due to propagation delays such as those in the ionosphere, the peak locations for signals in L1 and L2 may not coincide in time, phase, and frequency. A proper adjustment is required when attempting to combine L1 and L2 coherently.
- *Peak interpolation*: Due to the discrete nature of search grids, the true peak may lie between two search points. An interpolation in time and frequency may raise the gain by as much as 3 dB. The coherently added partial sums of T_3 are finally added non-coherently (in power) up to T_4 for all search points simultaneously per search tile.
- **Handover to tracking**: Once the signal accumulated at a search point exceeds the detection threshold, a double-check is applied. When the signal detection is confirmed, the peak location in time and frequency is used to initiate the subsequent tracking loop for this satellite. The search engine is then reset for another satellite. If no signal is detected for a search tile, the search engine is then reset to another search tile. If the search tiles are exhausted, the search moves on to another satellite in the search list.

3 | KEY ISSUES AND ENABLING TECHNIQUES

Key operations that enable coherent combining and long coherent integration are illustrated in Figure 3. The short-term correlations per one ms are represented by the yellow curves, which are buried in the noise represented by the purple curves. As shown, the underlying correlation peak undergoes two changes, namely, the peak location migrates in code phase (indicated by the green curve) due to code

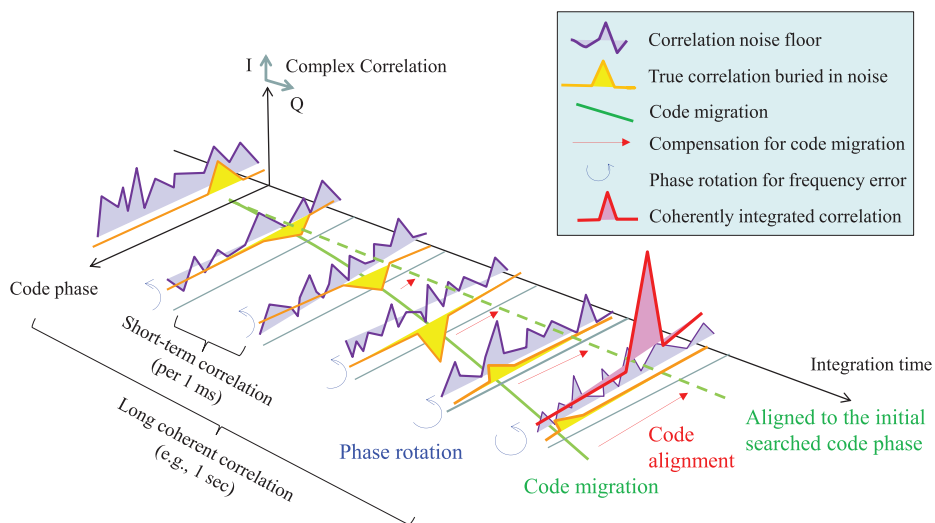


FIGURE 3 Illustration of key operations for coherent combining and long coherent integration (CCLCI)

rate errors, and the complex correlation peaks do not maintain the same orientation in the I-Q plane, but rotate due to frequency errors.

Straightforward summing up of all short-term correlations may not amount to the desired result because the individual peaks do not line up in time and the complex peak values are out of phase. Two major operations shown in Figure 3 are code alignment (indicated by the red arrows) so all peaks are aligned to the initially searched code phase, and phase rotation (indicated by the blue arrowed arcs) so the complex peak values are constructive. These and other operations are necessary so that the signal finally stands out above the noise floor (indicated by the pink curve).

3.1 | Enabling Technique 1: Long Coherent Integration in Stages

As shown in Figure 4, the sampling rate is f_s and each short-term correlation involves N samples over an interval of $T_1 = N\Delta t_s$ with $\Delta t_s = 1/f_s$. It can be shown that the m -th short-term correlation between t_m and t_{m+1} , denoted by c_m , can be written as:

$$c_m = Ae^{j\phi_0} N \frac{\text{sinc}(\pi\Delta f N\Delta t_s)}{\text{sinc}(\pi\Delta f \Delta t_s)} R(\Delta\tau_m) e^{j2\pi\Delta f [(m-1)N + \frac{N-1}{2}]\Delta t_s}, \quad m = 1, 2, \dots, M \quad (1)$$

where A is the signal amplitude and ϕ_0 is the phase difference between the incoming signal and carrier replica at t_m .

The short-term correlation c_m may be small if the signal is weak with a small A , or relatively small as compared to the interference signal not shown in (1). The correlation function $R(\Delta\tau_m)$ in Equation (1) is ideally of a triangular shape of unity height and suffers from an irreversible loss $R(\Delta\tau_m) = 1 - |\Delta\tau_m|/T_c < 1$ due to the timing error $|\Delta\tau_m| \neq 0$. In acquisition, a tolerable error is typically chosen to be $\Delta\tau_m = \tau - \hat{\tau} \leq \frac{1}{2}T_c$, where T_c is the code chip duration. This choice is determined by the code structure.

Similarly, the *sinc*-function in Equation (1) represents another irreversible loss due to frequency error Δf . To limit the loss, the tolerable error is typically chosen such that $\Delta f N\Delta t_s \leq \frac{1}{2}$. Clearly, it is determined by frequency search spacing and integration length, which our algorithm can control.

If the long integration is performed directly over T_2 , the required frequency resolution is $1/(2T_2)$, inversely proportional to the integration interval, which significantly increases the number of search steps. In addition, the input data rate is very high at f_s . A more practical approach is to perform long coherent integration in two stages. In the first stage, short-term correlations would be performed for the input samples at high rate (f_s) over T_1 at coarse frequency search bins with spacing of

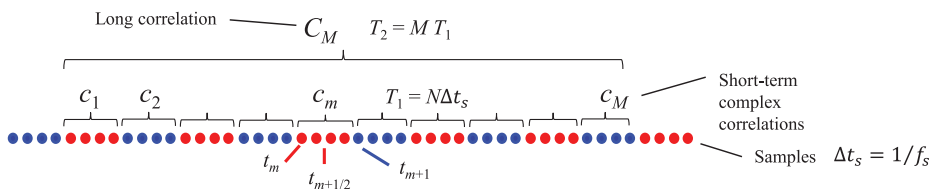


FIGURE 4 Division of long integration (C_M) into multiple short-term correlations (c_m , $m = 1, 2, \dots, M$)

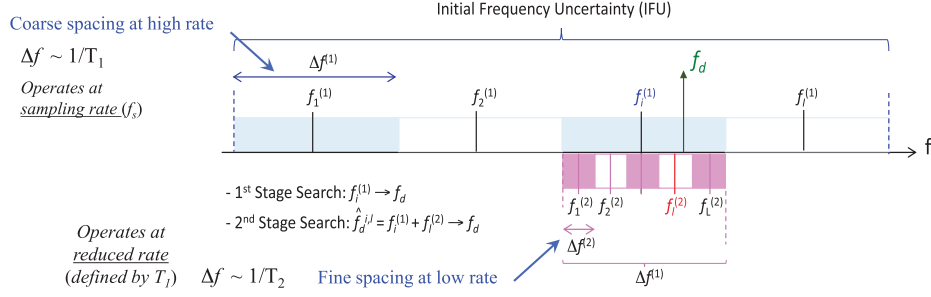


FIGURE 5 Coarse frequency search (1st stage) and refined frequency search (2nd Stage)

$1/(2T_1)$. In the second stage, the short-term correlations, now at a lower data rate ($1/T_1$ instead of f_s), would be further added up to T_2 at refined frequency search bins with spacing of $1/(2T_2)$ as shown in Figure 5.

3.2 | Enabling Technique 2: Phase Rotation for Coherent Integration

The individual short-term correlations c_m in Equation (1) can be added up over M periods into the long coherent integration C_M so as to boost the weak amplitude A and make up the irreversible losses due to $\Delta\tau$ and Δf . C_M can be shown to have the following form:

$$C_M = \sum_{m=1}^M c_m = A e^{j\phi_0} N \frac{\text{sinc}(\pi \Delta f N \Delta t_s)}{\text{sinc}(\pi \Delta f \Delta t_s)} \sum_{m=1}^M R(\Delta\tau_m) e^{j2\pi \Delta f [(m-1)N + \frac{N-1}{2}] \Delta t_s} \quad (2)$$

Due to the frequency error Δf , each short-term correlation is subject to an unknown phase rotation, which is the last term of Equation (2). We can obtain an estimate of this frequency error through frequency search. As shown in Figure 5, the refined frequency search bin $f_i^{(2)}$ around a coarse frequency search bin $f_i^{(1)}$ provides an estimate of the underlying frequency error as:

$$\Delta \hat{f} = f_d - f_i^{(1)} \approx f_i^{(2)} \quad (3)$$

Then, the phase-rotated long coherent integration can be written as:

$$C_M^{i,l} = \sum_{m=1}^M c_m^i \exp\{-j2\pi \Delta \hat{f} t_{m+\frac{1}{2}}\} = \sum_{m=1}^M c_m^i \exp\{-j\pi f_i^{(2)} (t_m + t_{m+1})\} \quad (4)$$

The phase rotation in Equation (4) can be implemented in hardware as a carrier numerically-controlled oscillator (NCO) for a given frequency $\Delta \hat{f}$. Alternatively, it can be implemented in software using the fast Fourier transform (FFT), which is equivalent to multiplying the short-term correlations with complex exponentials (phase rotation) for compensation at a refined frequency. The use of the FFT to perform the phase rotation in Equation (4), which is equivalent to Doppler frequency removal, is applied in double-FFT high-sensitivity acquisition (Jiménez et al., 2006), block-accumulating coherent integration over extended interval (BACIX; Yang & Han, 2006), and synthesized Doppler frequency hypothesis testing (SDHT; Kong, 2015). The FFT can be replaced with the chirp or fractional Fourier transform to deal with high dynamics (Wu et al., 2015).

3.3 | Enabling Technique 3: Compensation for Code Migration

Driven by a non-zero code Doppler, the code phase of an incoming signal migrates from one search point to a neighboring one while the local code replica is fixed at the initial point. In the tracking mode, the code replica is adjusted constantly to catch up with the incoming signal. In the acquisition stage, however, a code replica is prepared per frequency bin with a potential maximum frequency error being a half of that bin. The code Doppler error is not an issue as long as the code migration stays within a grid point. For any integration interval over which code migrates across search points, less and less signal accumulation appears at the original search point but more and more on a neighboring one, which delimits an effective coherent integration for each given residual Doppler.

To exemplify the effect at $L1 = 1,575.42$ MHz, consider an example with $T_1 = 1$ ms for a carrier Doppler error of $f_d = 250$ Hz, the code Doppler error at a chipping rate of $f_{chip} = 5.115$ mcps is $f_{chip} \cdot f_d / L1 = f_d / 308$, which translates to a code migration rate of 0.8116 chips/sec. In other words, it takes about 0.2, 0.4, and 0.8 sec for the peak to migrate by $1/4$, $1/2$, and one full chip. Residual Doppler causes the complete migration across a code phase search bin after 1.6 sec, and each code phase search point dominates about 0.8 sec as shown in Figure 6.

In Figure 6(a), five consecutive code phases are color-coded and a signal starts at Code Phase 3 (red) and sweeps through Code Phase 4 (black) and then Code Phase 5 (pink). Code Phase 4 (the black curve) takes over Code Phase 3 (the red curve) at 0.65 sec, which is, in turn, taken over by Code Phase 5 (the pink curve) at 1.25 sec as shown in Figure 6(b). In this example, the long integration period is 2 sec and the refined Doppler search bin is 0.25 Hz. With a 5-ms increment being the data bit interval, the contribution to the cumulative peak of coherent integration per data bit is shown in Figure 6(c) for different code phases.

The general triangle shape in Figure 6(b) is the rising and falling of correlations when the code migrates through different phases. Note that on top of the triangle shape are stair-like variations with a stair width of 0.08 sec. There are eight stair steps over each $1/2$ chips, which correspond to eight samples averaged prior to a simple 8:1 decimation in down-sampling ($f_s = 16f_{chip}$). A smooth response is expected if a low-pass filtering is used.

There are different methods to compensate for code Doppler as summarized below (Foucras et al., 2014):

- **Method 1: Code Doppler compensation on spreading code sequences:** One technique is to generate a local spreading code for each possible incoming Doppler frequency (Ziedan, 2006). The method is very expensive in terms of

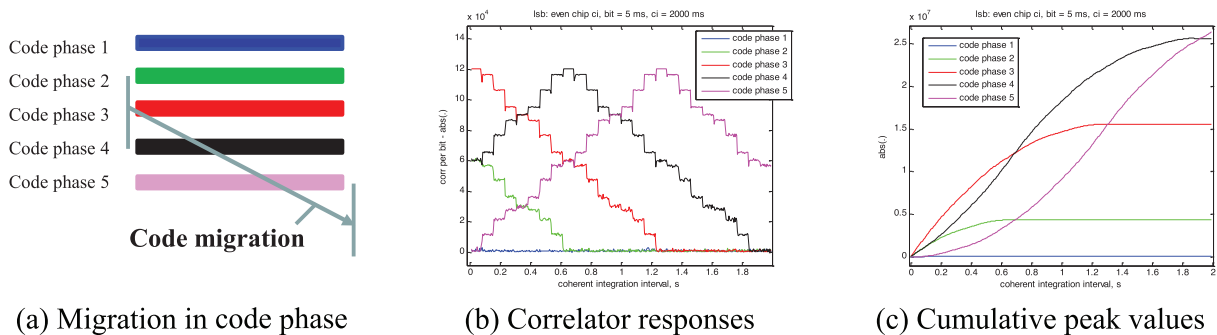


FIGURE 6 Illustration of code migration and its effect on correlation peak values

computation and storage. In another method, for every Doppler frequency estimate, an interpolation is made on both the received signal and the local replica to ensure that there is exactly one full spreading code period present in the coherent integration interval (Psiaki, 2001). For FFT-based correlation, the code delay induced by code Doppler can be compensated for in the frequency domain by multiplying the FFT of a local spreading code by a complex exponential corresponding to the delay (Akopian, 2001; Krasner, 1997).

- **Method 2: Code Doppler compensation on correlator outputs:** One technique is to choose the pickup points in coherent integration results to compensate for phase sliding based on determining the amount of code phase shift from the estimated code Doppler (Jiao et al., 2012). Another technique is the de-skewed short-term correlator (Betz, 1984), implemented in DirAc, which resamples/interpolates the short correlators for alignment. Migration of correlation peak, i.e., shifting the correlation function (Guo et al., 2017) can be compensated for in the frequency domain using the Keystone transformation (Li et al., 2006) in much the same way as range migration in delay-Doppler imaging of moving targets by radar.

In the present implementation, we use the approach of re-indexing short-term correlations based on the present code Doppler estimate. For a second stage frequency search bin $f_i^{(2)}$ around the coarse frequency search bin $f_i^{(1)}$, the corresponding code Doppler (the code Doppler difference between the incoming signal f_d and the local replica driven by $f_i^{(1)}$) is given by:

$$f_{chip}^l = f_{chip} \frac{f_i^{(2)}}{f_i^{(1)}} \quad (5)$$

where f_{chip} is the nominal chip rate.

Denote the code phase of the first chip in each short-term correlation along the long coherent integration interval by $n_{chip}(m)$, $m = 1, 2, \dots, M$, which evolves from the initial code phase $n_{chip}(1)$ driven by the code Doppler f_{chip}^l as:

$$n_{chip}(m) = n_{chip}(1) + (m-1)T_{ms} f_{chip}^l \quad (6a)$$

$$n_{chip}(m) = n_{chip}(1) + (m-1)T_{ms} f_{chip} \frac{f_i^{(2)}}{f_i^{(1)}} \quad (6b)$$

In terms of code search bins, it can be written as:

$$n_{bin}(m) = \text{round} \left(\frac{n_{chip}(1) + (m-1)T_{ms} f_{chip} \frac{f_i^{(2)}}{f_i^{(1)}}}{b_{chip}} \right) \quad (6c)$$

where b_{chip} is the search bin width in chips. For example, when the correlator spacing is a sampling interval, $b_{chip} = f_{chip}/f_s = 5.115/56.32 \approx 0.1$ chips/bin where $f_s = 56.32$ MHz is the sampling rate. The short-term correlations c_m^i at $n_{bin}(m)$ for $m = 1, 2, \dots, M$ are then selected for the search bin $f_i^{(2)}$ to perform the residual frequency compensation in coherent integration (4).

3.4 | Enabling Technique 4: Compensation for Frequency Divergence between Sidebands

The upper and lower sideband signals, when treated separately as two BPSK signals, have a different center frequency. As such, they are subject to different Doppler frequency shift and frequency-dependent dispersive effects (Rushanan &

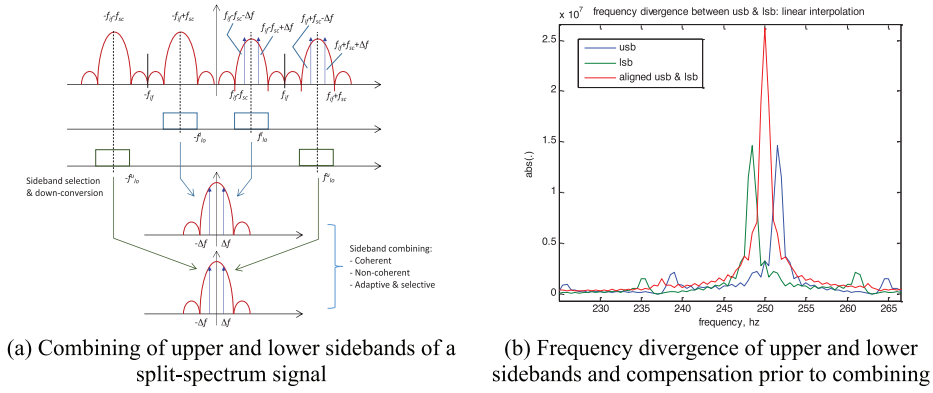


FIGURE 7 Frequency divergence and compensation

Winters, 2010). In particular, when the interval for coherent integration is long enough to allow the code phase to migrate across a large portion of a code chip, the code migration introduces an amplitude modulation to the short-term correlations. The amplitude modulation can also shift the frequency of the upper and lower sidebands.

The spectra of the upper and lower sidebands are complex conjugates of each other. The above-mentioned frequency shifts are actually in opposite directions, leading to a frequency offset or frequency divergence between the upper and lower sidebands. The frequency offset becomes detrimental to signal combining when it is larger than the refined frequency resolution. Frequency alignment is therefore necessary to remove the frequency offset between the sidebands so as to reap more gain out of sideband combining.

As shown in Figure 7(a), the upper and lower sidebands of an IF signal are bandpass-filtered and down-converted to the baseband separately. Once in the baseband, they are processed independently and then combined. Figure 7(b) shows an example of combining upper and lower sidebands with frequency divergence and its compensation. In this example, $T_1 = 1$ ms (the short-term correlation interval), $\Delta f = 500$ Hz (the frequency bin), $\Delta \tau = 0.5$ chips (the code phase spacing), $f_d = 250$ Hz (the maximum frequency error for T_1), $T_2 = 5$ ms (the bit interval), and $T_3 = 1,000$ ms (the long coherent integration interval with 0.5 Hz required for post-correlation frequency compensation).

The Doppler shifts experienced by the upper and lower sidebands, denoted by f_d^{usb} and f_d^{lsb} , respectively, can be written as:

$$f_d^{usb} = -\frac{v}{c}(f_L + f_{sc}) = -\frac{v}{c}f_L - \frac{v}{c}f_L \frac{f_{sc}}{f_L} = f_d + f_d \frac{f_{sc}}{f_L} \quad (7a)$$

$$f_d^{lsb} = -\frac{v}{c}(f_L - f_{sc}) = -\frac{v}{c}f_L + \frac{v}{c}f_L \frac{f_{sc}}{f_L} = f_d - f_d \frac{f_{sc}}{f_L} \quad (7b)$$

$$f_d = -\frac{v}{c}f_L \quad (7c)$$

where c is the speed of light, v is the range rate, f_L is the carrier frequency (L1 or L2), f_{sc} is the subcarrier frequency, and f_d is the Doppler shift experienced at the carrier (the band center).

From Equations (7a) and (7b), the difference in Doppler shifts (frequency divergence) experienced by the upper and lower sidebands is:

$$DF = f_d^{usb} - f_d^{lsb} = 2f_d \frac{f_{sc}}{f_L} = \begin{cases} 2 \times \frac{10.23}{1575.42} f_d = 0.0130 f_d \text{ Hz, for L1 signals} \\ 2 \times \frac{10.23}{1227.60} f_d = 0.0167 f_d \text{ Hz, for L2 signals} \end{cases} \quad (8)$$

Note that the Doppler frequency shift experienced by each sideband is only a few Hz (e.g., 1.625 Hz for $f_d = 250$ Hz at L1), which is not visible when $T_{LCI} < 308$ ms because $\Delta f^{(2)} > 1.625$ Hz. However, it is visible when the refined frequency search bin spacing is on the order of 1 Hz ($T_{LCI} = 500$ ms) and separable on the order of 0.5 Hz ($T_{LCI} = 1,000$ ms). Clearly, the frequency divergence in this example exceeds the frequency resolution and thus needs to be accounted for prior to combining.

Considering the frequency divergence at different sidebands, bringing Equations (7a) and (7b) into Equation (8) gives:

$$\Delta f^{usb} = f_d^{usb} - f_i^{(1)} = f_d + f_d \frac{f_{sc}}{f_L} - f_i^{(1)} \quad (9a)$$

$$= \left(f_l^{(2)} + f_i^{(1)} \right) + \left(f_l^{(2)} + f_i^{(1)} \right) \frac{f_{sc}}{f_L} - f_i^{(1)} \quad (9b)$$

$$= f_l^{(2)} + \left(f_l^{(2)} + f_i^{(1)} \right) \frac{f_{sc}}{f_L} \quad (9c)$$

An additional term appears in the compensation (4) for the upper sideband signal as:

$$USB_C_M^{i,l} = \sum_{m=1}^M c_m^i \exp \left\{ -j2\pi \left[f_l^{(2)} + \left(f_l^{(2)} + f_i^{(1)} \right) \frac{f_{sc}}{f_L} \right] t_{m+\frac{1}{2}} \right\} \quad (10)$$

Similar equations for the lower sideband signal can be written as:

$$\Delta f^{lsb} = f_d^{lsb} - f_i^{(1)} = f_d - f_d \frac{f_{sc}}{f_L} - f_i^{(1)} = f_l^{(2)} - \left(f_l^{(2)} + f_i^{(1)} \right) \frac{f_{sc}}{f_L} \quad (11a)$$

$$LSB_C_M^{i,l} = \sum_{m=1}^M c_m^i \exp \left\{ -j2\pi \left[f_l^{(2)} - \left(f_l^{(2)} + f_i^{(1)} \right) \frac{f_{sc}}{f_L} \right] t_{m+\frac{1}{2}} \right\} \quad (11b)$$

In the above analysis, the group delay between the sidebands (due to signal propagation and/or receiver antenna/RF artifacts) is not considered. However, for a large sideband separation, the group delay can no longer be ignored and needs to be factored in for coherent combining. Hence, a search is added in the delay space similar to coherent combining of L1 and L2 as described in Section 3.6.

3.5 | Enabling Technique 5: Estimation and Correction of Symbol Signs

Modern GNSS signals contain data and data-less (pilot) signals. In Galileo E5, for instance, data and pilot signals are separately modulated on I- and Q-components. In GPS, on the other hand, the time division data multiplexing (TDDM) scheme is used for M-code (Dafesh et al., 2002) in which the data bits and data-less bits are put on the odd and even chips separately.

It is straightforward to apply coherent integration to pilot signals, i.e., data-less even chips (Dafesh et al., 2002). A conservative approach can apply non-coherent integration to data-modulated signals (odd chips) since the signs of modulated data symbols are unknown. Yet, such an approach results in a significant squaring loss, which can be detrimental for weak signal and strong interference scenarios. To boost the signal strength, it is possible to apply sign-guessing/correction when going from bit interval T_2 to long coherent interval T_3 (Soloviev & Dickman, 2011, 2014; Soloviev et al., 2008, 2012; Yang & Han, 2006, 2007).

One way to guess and correct the bits is to find their signs such that the accumulated signal power is maximized:

$$\{\hat{b}_i^*\} = \arg \max_{\{\hat{b}_i = \pm 1\}} \left(ci_N^{ou}(\{\hat{b}_i\}) + ci_N^{eu} \right)^2 + \left(ci_N^{ol}(\{\hat{b}_i\}) + ci_N^{el} \right)^2 \quad (12)$$

where the superscripts o and e stand for the odd chips (data-modulated) and even chips (data-less) while the superscripts u and l stand for the upper and lower sidebands, respectively; ci_N is the value of chips integrated over N data bits, and \hat{b}_i is the guessed sign for the data bit b_i .

Simulation results indicate that the successful rate of sign guessing depends strongly on the signal energy per data bit. Maximization over multiple data bits may reduce the bit error rate. Yet, it cannot guarantee the uniqueness of each guessed bit sequence because of the effect of residual Doppler errors. At the low data rate of 50 bps, the approach seems useful but becomes less practical at the high data rate of 200 bps or for extremely weak signals.

For GNSS signals with high symbol rate data and secondary codes that can change their sign within each primary code period, advanced methods that are tailored to individual code inner structures can be employed (Borio, 2008; Leclère et al., 2017; Svaton & Vejražka, 2020).

3.6 | Enabling Technique 6: Coherent Combining of Multi-Frequency Signals

A natural extension of the above approach is to combine signals at multiple frequencies to further improve the acquisition performance. Signals at individual frequencies are first accumulated independently using the combination of the coherent and non-coherent integration strategies previously described.

The accumulation results in the form of signal energy vs. code phase and Doppler shift are then combined. However, ionospheric delays can create differences between code phases at L1 and L2 in excess of the code search grid size. Hence, an adjustment is performed to avoid energy losses.

The delay search space is formed to include the worst-case ionospheric delay between L1 and L2 signals. For each search bin, L2 accumulation results are first adjusted via the re-indexing of code phase search bins. For example, to adjust for the negative delay of one code chip, the code bin index is incremented by two (for a half-chip spacing). The re-indexing of frequency bins is not required.

Then, L1 and adjusted L2 accumulated signal energies are added non-coherently. The adjustment bin that maximizes the overall signal energy is used to determine the acquired code phase and Doppler frequency. Coherent integration is possible but it requires an additional search to compensate for phase errors between L1 and L2, which is a trade-off between performance gains vs. extra computations. An example of coherent combining E5aI, E5aQ, E5bI, and E5bQ in real data can be found in Yang and Soloviev (2016).

4 | ANALYSIS OF DIRECT ACQUISITION PERFORMANCE

The ability of long coherent integration is first shown with an example. Correlation functions over search space are analyzed and, in particular, the appearance of secondary peaks for special cases. Embedded acquisition performance under strong interference is demonstrated. Comparisons of CI and CI/NCI schemes are presented to show implementation trade-offs.

4.1 | Ability of Long Coherent Integration

The ability to perform long coherent integration over one second is demonstrated in the example shown in Figure 8. A BOC(10, 5) signal under an open-sky condition is generated by a Spirent GPS RF Simulator and down-converted to baseband and sampled by a transform-domain instrumentation GPS receiver (TRIGR) that uses a stress compensated (SC)-cut quartz OCXO at 10 MHz (Gunawardena, 2007). The true frequency of the signal is marked with a black arrow in Figure 8(a).

A coarse frequency search grid is chosen to have three bins spaced by 250 Hz. Bin 1 (purple) is smaller while Bin 3 (red) is larger than Bin 2 (green) by 250 Hz. The short-term 1-ms correlations have an effective frequency coverage of ± 500 Hz. As a result, all three frequency bins are responsive to the signal, but the strongest is from Bin 2, which is the closest to the true signal. The refined frequency searches from the three coarse bins all converge to the same estimate as shown in Figure 8(b).

However, code migration occurs for the three coarse bins as shown in Figure 8(c). The code search grid has a spacing about 1/10 of a chip. Since Bin 2 is closest to the true signal, the frequency error is small for code and carrier replicas generated at this frequency bin. There is practically no code migration and the correlation peak stays at the same code phase index (the green curve) when integrated longer and longer over time.

On the other hand, since the frequency of Bin 1 is smaller than the true signal, its frequency error is negative. As the signal is stretched, the code phase is delayed. The short-term correlation peak moves to a smaller and smaller index for subsequent correlation intervals (the purple curve). Similarly, the frequency of Bin 3 is larger than the true signal, its frequency error is positive. As the signal gets squeezed, the code phase is advanced. The short-term correlation peak moves to a larger and larger index for subsequent correlation intervals (the red curve).

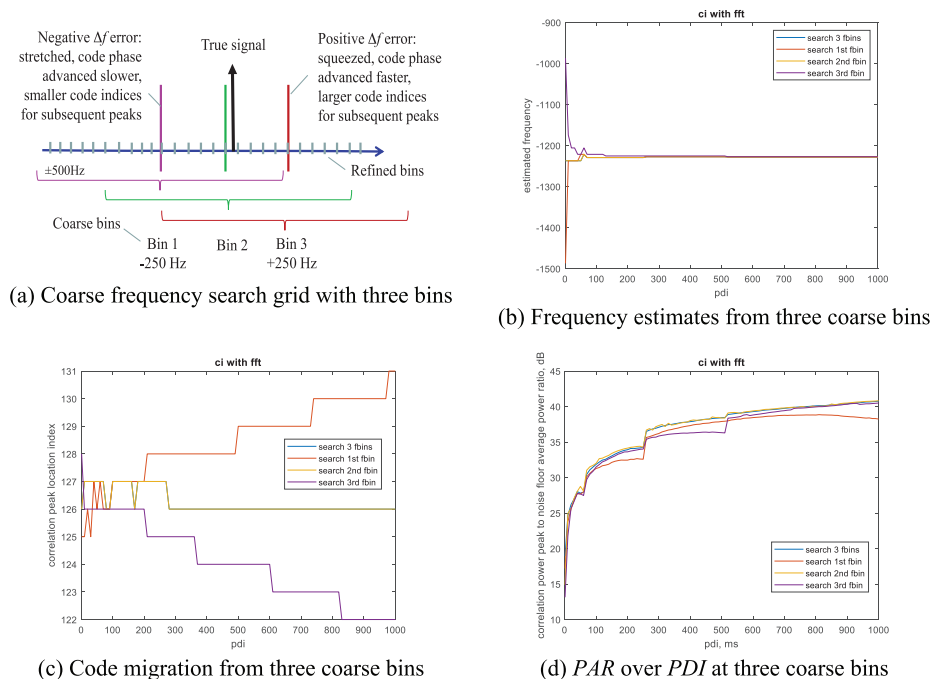


FIGURE 8 Example of long coherent integration over 1 second at three frequency search bins

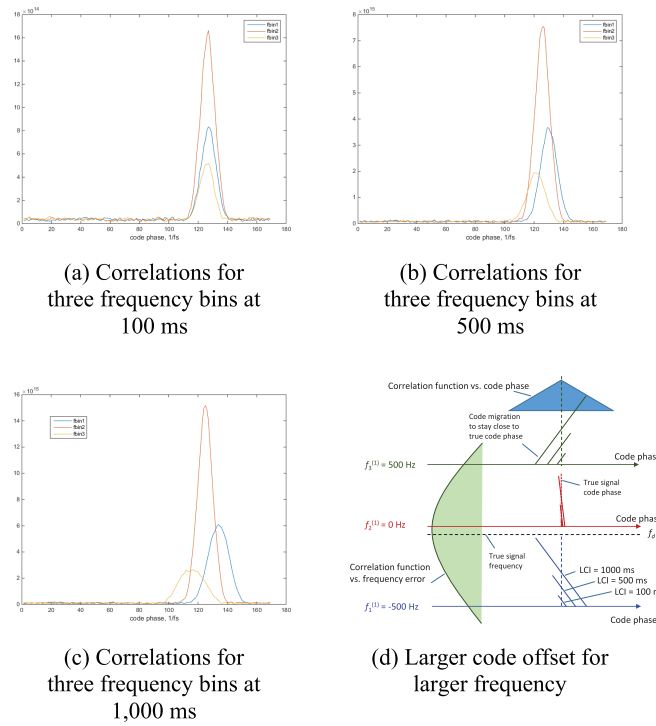


FIGURE 9 An illustrating example of code migration

The correlation *peak-to-noise floor average power ratio* (PAR) as a function of *pre-detection integration* (PDI) = 1 ms to 1,000 ms is shown in Figure 8(d) at the three coarse frequency bins. The results demonstrate long coherent integration over 1 sec. Note that the step jumps at PDI = 64, 256, and 512 in Figure 8(d) are caused by frequency resolution improvement. In the implementation, the phase rotation specified in Equation (4) is implemented with the FFT, zero-padded to the next power of two of its length. A higher resolution means a smaller loss due to reduced frequency errors.

Another example explaining code migration due to frequency error is shown in Figure 9. As shown, the three frequency bins all capture part of the signal energy. For the 1-ms correlations, their frequency response has the first nulls at ± 1 kHz. Any two adjacent bins, which can be as large as 500 Hz apart, have a non-trivial gain to the incoming signal.

However, the correlation peak values for different frequency bins do not always coincide in code phase, but rather are separated more and more as the integration interval increases as shown by partial sums of correlation plotted against code phases at PDI = 100, 500, and 1,000 ms in Figure 9(a), 9(b), and 9(c), respectively.

Figure 9(d) illustrates the code migration process. The code Doppler rate is 0.811 chips/sec for a frequency error of 500 Hz. At those frequency bins, the code replicas have to start from larger offset code phases and then are shifted by their respective code Doppler so as to align with the incoming code phases.

Ideally, the signal strength increases linearly with the integration time. The linearity, however, may not hold up in reality due to implementation impairments. Figures 10(a) and 10(b) show the partial sums of coherently integrated odd and even chips for upper and lower sidebands on L1 and L2 for PRN7, respectively.

First note that the partial sums of the lower even (LE) are higher than the upper even (UE) in both L1 and L2, which are attributed to channel asymmetry. The RF

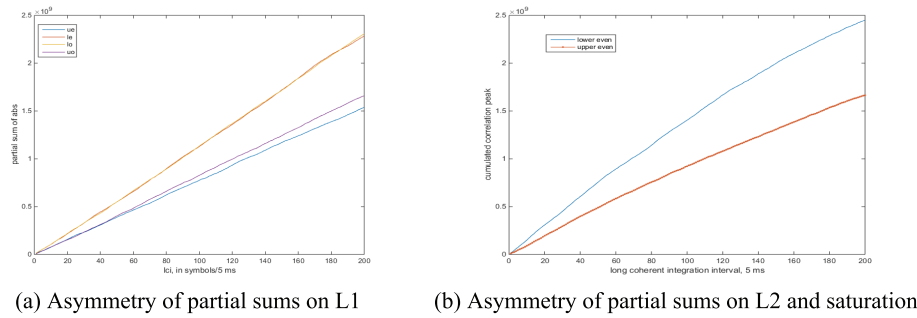


FIGURE 10 Impairments affecting effective gain of long coherent integration

front-end (RF FE) used in our data collection was not designed for the bandwidth of BOC(10, 5); furthermore, the bandwidth of an upper sideband extraction filter is narrower than that for a lower sideband. For L1 in Figure 10(a), the lower even (LE, indicated in orange) and lower odd (LO, indicated in yellow) have about the same magnitude whereas the upper odd (UO, indicated in purple) is slightly higher than the upper even (UE, indicated in blue).

It is rather clear in Figure 10(b) that the partial sums start to flatten out, which is due to uncompensated frequency error and clock instability that start to manifest in long integration. In addition to frequency drift and code migration, this saturation effect is another limiting factor as to how long the coherent integration can last. Due to saturation, the small increase in signal strength may not justify the additional amount of resources needed to extend the coherent integration further—a diminishing return aspect to be taken into account in the design trade-offs.

4.2 | Analysis of Correlation Functions over Search Space

Figure 11 shows the correlation functions integrated over one second over a time-frequency search grid consisting of three coarse frequency bins (500-Hz spacing) expanded to 3,000 fine frequency bins (0.5-Hz spacing), and 169 code phases (1/10-chip spacing). It was under an open-sky condition for PRN = 7 on L1, which had the true Doppler $f_d \approx -477$ Hz. Three coarse frequency search bins were at $f_i^{(1)} = [-900, -400, 100]$ Hz. The residual frequency error was 77 Hz from the second bin.

The even chips on lower and upper sidebands were coherently integrated over 1 s as shown in Figure 11(a) and 11(b), respectively. For the odd chips on lower and upper sidebands, they were coherently integrated to 5 ms (a data bit duration) and then non-coherently to 1 s as shown in Figure 11(c) and 11(d), respectively. Additional examples for PRNs on L1 and L2 from different initial conditions can be found in Yang et al. (2020b).

Figure 12 compares the correlations of even chips, odd chips, and their combinations. In the code-phase domain, Figure 12(a) shows the correlation functions of even chips that were coherently integrated to 1 second for all frequency search bins. Figure 12(b) shows the correlation functions of odd chips bitwise coherently and then non-coherently integrated to 1 second.

As shown, both the even and odd chip correlations had about the same peak value, size, and shape. However, the noise floor of the coherently integrated even chips in Figure 12(a) proved to be much lower than that of odd chips in Figure 12(b).

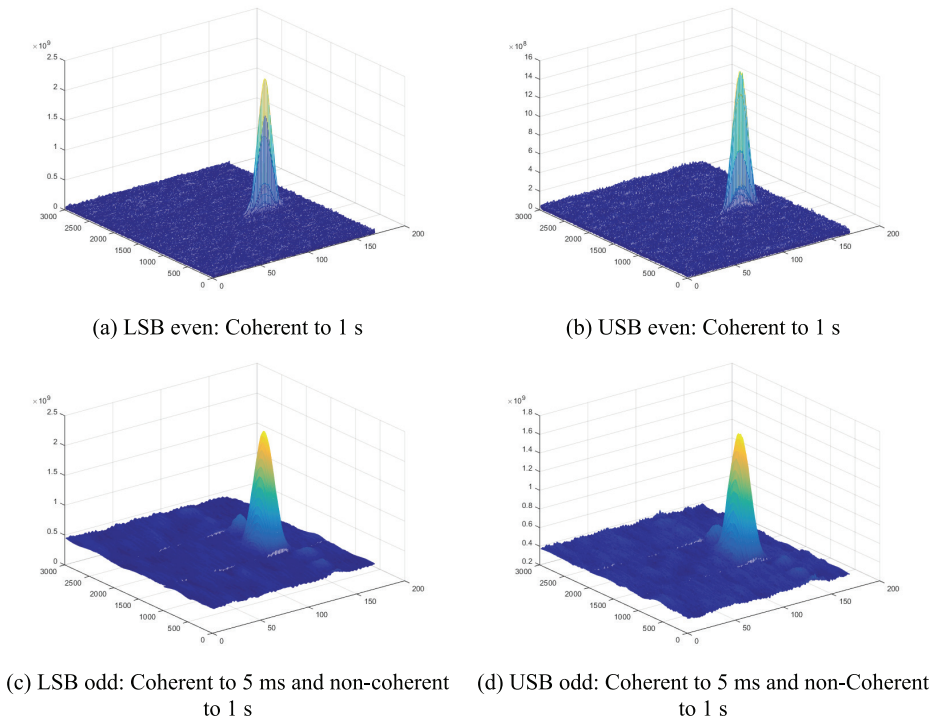


FIGURE 11 1-s correlations over time-frequency search grid

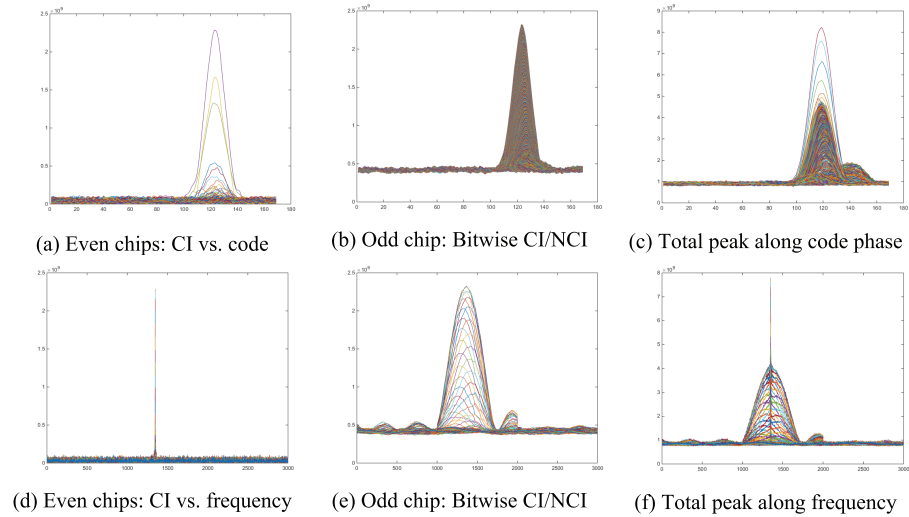


FIGURE 12 Coherent vs. coherent/non-coherent integrations of even and odd chips

In contrast, Figure 12(c) shows the non-coherent integration of the even and odd chips from both L1 and L2, which had a peak four times higher.

In the frequency domain, Figure 12(d) shows the correlation functions of even chips coherently integrated to 1 second for all searched code phases. Figure 12(e) shows the correlation functions of odd chips bitwise coherently and then non-coherently integrated to 1 second. As shown, both the even and odd chip correlations had about the same peak value. However, the noise floor of the coherently integrated even chips in Figure 12(d) was much lower than that of odd in Figure 12(e).

Besides, the coherently integrated even chips in Figure 12(d) had a very narrow peak with the first nulls at ± 0.5 Hz. In contrast, the non-coherently integrated odds had an elevated noise floor and its mainlobe was wide at ± 200 Hz corresponding to the bit duration of 5 ms. It indirectly points to the benefits of coherent over non-coherent integration. Figure 12(f) shows the non-coherent integration of even and odd chips from both L1 and L2, which had a peak four times higher. It also shows secondary peaks in frequency, which is explained next.

4.3 | Analysis of Secondary Peaks

Secondary peaks develop in the special case in which the true signal appears in the middle of two adjacent frequency bins. Consider PRN = 7 on L1 whose true Doppler is about $f_d = -477$ Hz and four coarse frequency search bins are chosen at $f_i^{(1)} = [-1,227, -227, 273]$ Hz. The true signal would be 250 Hz away from the middle two bins.

Figure 13(a) shows the non-coherent integration of the bitwise correlations of odd chips combined from upper and lower sidebands where a strong secondary peak appeared along the code phase. The color-coded correlation surface is shown in Figure 13(b), and the cuts along the frequency axis for two code phases and the cuts along the code phase axis for two frequency bins are shown in Figure 13(c) and 13(d), respectively. Note that the two USB curves are lower than the LSB ones due to channel asymmetry as explained in Figure 10.

The peak along the frequency in Figure 13(c) was made of two halves: The left half peaked at an index of 2,000 (-476.5 Hz) and had its left null at 1,600 (200-Hz offset) while the right half peaked at 2,001 (-477 Hz) and had its right null at 2,400 (also 200-Hz offset). The two halves together made a peak width of ± 200 Hz, corresponding to the data bit of 5 ms, as expected. Note that only a search at a negative

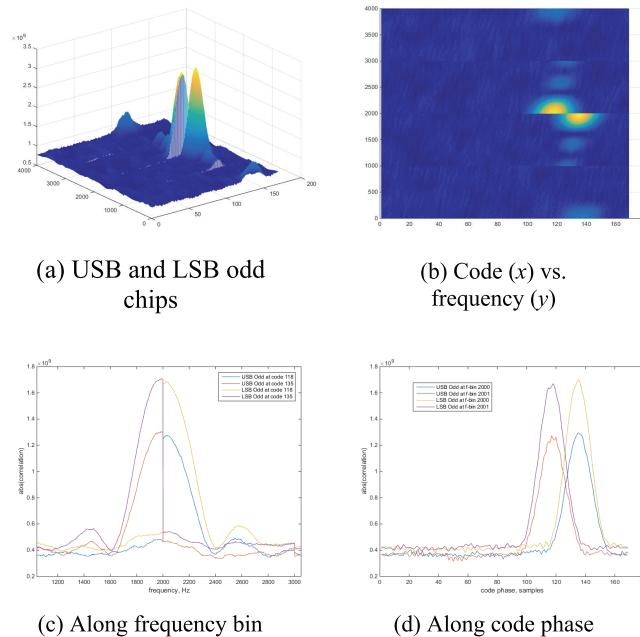


FIGURE 13 Bitwise correlations of odd chips on upper and lower sidebands: Secondary peaks when the signal straddles two frequency bins

frequency (refined frequency bin index smaller than 2,000) could produce the correct alignment for code phase 135 and similarly only a positive frequency (larger than index 2,001) could produce the correct alignment for code phase 118, which explains the sharp drop around 2,000.

However, two peaks of comparable amplitude appeared along the code phase axis as shown in Figure 13(d). Namely, the 1-s non-coherent integration of bitwise coherent correlations of USB and LSB odd chips at Frequency Bin 2,001 provided the correct peak at code phase 118, while the non-coherent integration at Frequency Bin 2,000 produced a false peak at 135, which was off by 18 samples.

There are several reasons for this phenomenon. First, the frequency response of the bitwise coherent integration was so wide that it allowed many frequency bins to “compete,” so to speak. Second, when the true signal falls exactly in the middle of two adjacent coarse frequency search bins, it can be reached from the opposite direction, giving rise to spurious peaks. Third, a frequency search bin on the wrong side accumulates from a code phase also on the wrong side. For the example in Figure 13, the separation between the true and false peaks was twice the code phase drift over 1 s for a frequency error of 250 Hz, that is, $2f_{chip}/L1 \times f_d$ in chips or $2f_s/L1 \times f_d = 2 \times 56.32/1575.42 = 17.87$ samples. Further explanations and additional examples about spurious peaks can be found in Yang et al. (2020).

4.4 | Embedded Acquisition Performance under Interference

The generation of test scenarios subject to interference is shown in Figure 14. Interference signals were injected digitally to the BOC(10, 5) data (an M-prime code) generated by a Spirent GPS RF Simulator. The RF signal was recorded by a special GPS receiver, TRIGR (Gunawardena, 2007), from which the noise power was estimated as was the signal power, determined with the estimated C/N_0 and verified against the value in the configuration file of Spirent GPS RF Simulator.

As shown, two types of interference signals were injected. One was a *band-limited broadband* (BLBB) noise jammer within ± 10 MHz, which wipes out the band center where C/A-code and P(Y) code mainly reside so as to emulate a blue force electronic attack (Dominguez et al., 2016; Fishman & Betz, 2000; Holmes et al., 1999;

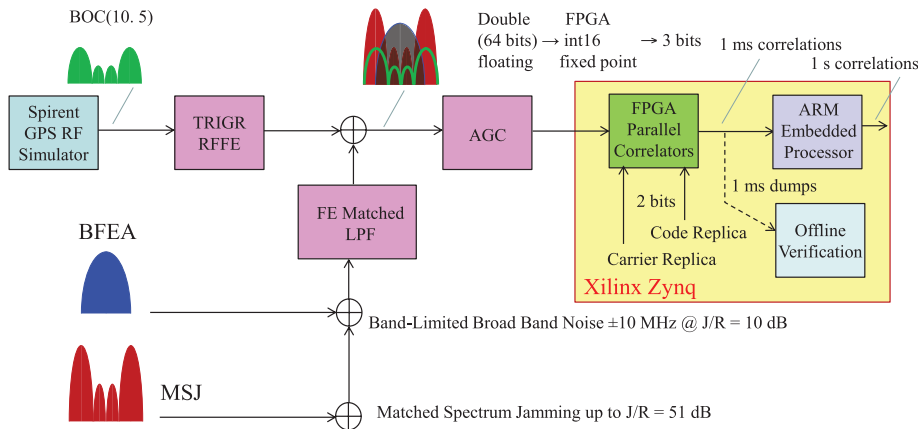


FIGURE 14 Block diagram of interference signal injection

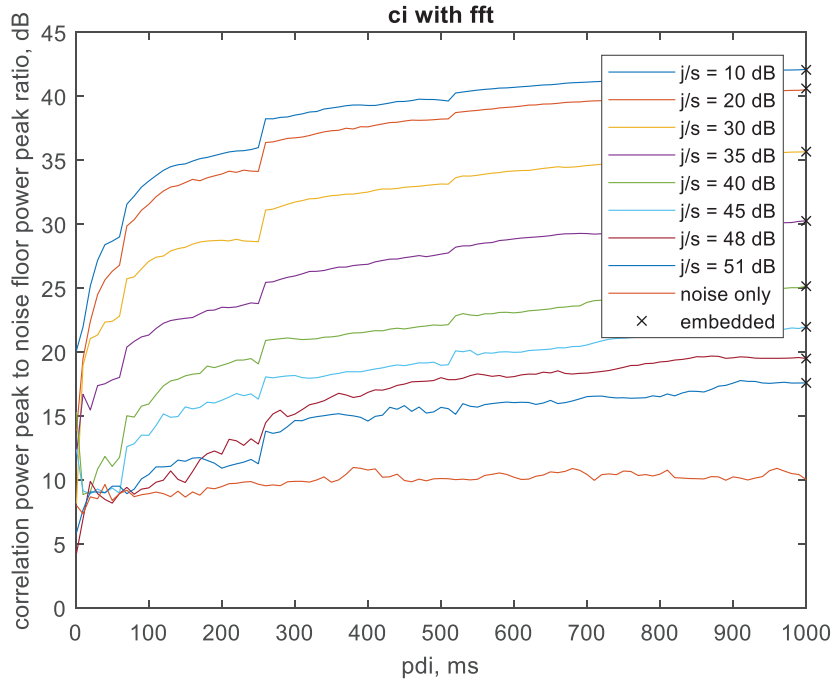


FIGURE 15 Peak-to-peak ratio of CCLCI vs. PDI for different J/S

Leclère et al., 2016; Ward, 2003b). A random noise was generated and passed through a low-pass filter and the samples were scaled so that the output noise power matched the desired *jamming-to-signal ratio* (J/S) of 10 dB. The other interference signal was a *matched-spectrum jammer* (MSJ) as another BOC(10, 5) with its strength adjustable up to J/S = 51 dB.

An automatic gain control was applied to the combined signal to avoid signal clipping and maintain it within the level for type conversion from double (64 bits) to integer (16 bits), which was then adaptively quantized to three bits for hardware correlation on a Xilinx Zynq (FPGA + ARM) card.

As shown in Figure 14, the 1-ms short-term correlations generated by FPGA-implemented parallel correlators as part of the first stage coarse frequency search are sent to the embedded ARM processor for coherent integration with the second stage refined frequency search. At the same time, the 1-ms short-term correlations are off-loaded for post-processing and verification.

Due to hardware limitations (e.g., the asymmetry of upper and lower sideband channels shown in Figure 10), only the even chips on the lower sideband were processed to illustrate the embedded SDR ability for long coherent integration. The performance of direct acquisition under interference is summarized in Figure 15. The correlation *peak-to-noise floor peak power ratio* (PPR) in dB (the y-axis) is shown as a function of PDI = 1 ms to 1,000 ms (the x-axis) for eight interference conditions with J/S = 10, 20, 30, 35, 40, 45, 48, and 51 dB, respectively, plus a noise-only case.

During each test run, the short-term correlations were dumped into a data file for offline verification. These short-term correlations were coherently integrated for different PDI, shown as the solid lines and color-coded for different J/S values in Figure 15. The embedded 1-s long coherent integration results output by the hardware are marked with crosses (×) in Figure 15. At PDI = 1,000 ms, the offline processing results matched well with those of embedded processing, demonstrating the CCLCI performance on hardware.

The time and frequency parameters obtained from the initial 1-s correlation, which was based on repeated replay of the signal samples stored in memory on the Xilinx Zynq card, were projected for live signals in subsequent 1-s correlations. The correlation peak was again clearly above the noise floor, indicating that the signal was indeed detected and the signal's time and frequency estimates were valid. However, the second 1-s correlation peak was not as sharp as the first one. It is understandable because the long coherent integration is very sensitive to frequency errors (need to be better than 0.5 Hz for 1-s correlation) and over the integration intervals, the signal parameters had changed due to signal dynamics and/or combined satellite and receiver clock drifts.

4.5 | Combined CI and NCI Implementation Trade-offs

The ability of CCLCI for 1-s coherent integration was demonstrated in embedded tests. It is of further interest to compare CCLCI with standard acquisition schemes based on short *coherent integration* (CI) cascaded with *non-coherent integrations* (NCI) as suggested by Pany (2020) to better understand the performance gain of CCLCI especially during radio frequency interference (RFI) and to provide insights for implementation trade-offs. Among the possible post-correlation or pre-detection integration schemes (Gómez-Casco et al., 2020), we consider here three different CI and NCI combinations with CCLCI as the baseline as:

- **Scheme 0:** CI = 1,000 ms and NCI = 0
- **Scheme 1:** CI = 5 ms (corresponding to high data rate of 200 Hz) and NCI = 200
- **Scheme 2:** CI = 20 ms (corresponding to low data rate of 50 Hz) and NCI = 50
- **Scheme 3:** CI = 100 ms and NCI = 10

The same embedded 1-ms correlations as Scheme 0 in Figure 15 were processed for Schemes 1, 2, and 3 and the results are shown in Figure 16(a), 16(b), and 16(c), respectively.

The case without signal (noise alone) was used to establish the baseline with the PPR, which was used as a metric rather than the usual PAR for performance evaluation. It is a choice of convenience (easy implementation and fast calculation). Typically, the PPR is lower than the PAR, thus this choice was on the conservative side. As a measured quantity, PAR is an estimate of the underlying SNR and may

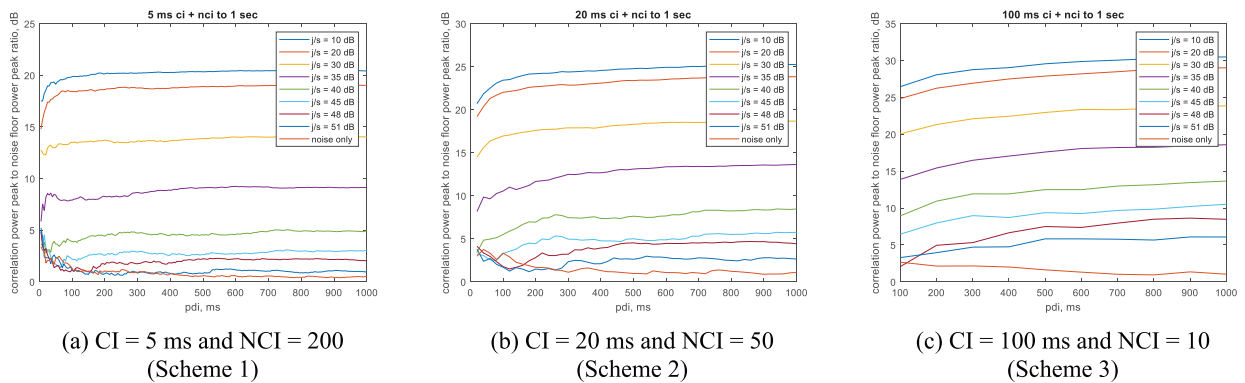


FIGURE 16 PPR vs. PDI of combined coherent and non-coherent integration schemes under different J/S

be used interchangeably with SNR in analysis. A simplistic analysis of the relative performance is presented below.

First, look at the noise-only case where no signal is present. For Scheme 0, the output PPR of CCLCI stabilized at 10 dB. For the combined CI/NCI schemes, it went from 4 ~ 5 dB down to 1 ~ 2 dB and became smaller for shorter CI and, asymptotically, it went to 0 dB for larger NCIs. This can be understood as NCIs provide an estimate of the noise power (variance) for all search points and it thus equalizes the peaks and valleys in the long run.

For Scheme 0 with coherent integration, the PPR proved to grow up even though at a gradually slower rates and after 500 ms, the gain may not have warranted the expensive computations in view of the diminishing return effect. For the combined CI/NCI schemes, their growth rates were smaller and even more so for shorter CIs. It practically stopped at 200 ms for CI = 5 ms in Scheme 1, 400 ms for CI = 20 ms in Scheme 2, and 600 ms for CI = 100 ms in Scheme 3, respectively. This indicates a practical limit on how long NCIs can be useful, especially for weak signals.

If a 5-dB or more margin in a PPR was required in test threshold for reliable detection, Scheme 0 could stop at 500 ms for $J/S = 51$ dB. Scheme 1 with CI = 5 ms could not detect a signal with $J/S > 51$ dB, but those with < 45 dB after 250 ms. Similarly, Scheme 2 with CI = 20 ms could not detect a signal with $J/S > 51$ dB, but those with < 40 dB after 200 ms. Finally, Scheme 3 with CI = 100 ms could not detect $J/S > 51$ dB (barely after 800 ms), but < 48 dB after 500 ms. This clearly shows the superior detection performance of Scheme 0 over the CI/NCI schemes.

Consider now the output of the PPR of the three combined CI/NCI schemes under $J/S = 10$ dB. The end PPR at 1 second was 21 dB for Scheme 1, 25 dB for Scheme 2, and 31 dB for Scheme 3, respectively. From CI = 5 ms, 20 ms, and 100 ms to 1,000 ms, the time factor was 200, 50, and 10 and the corresponding coherent processing gain was 23, 17, and 10 dB, respectively. Their difference relative to Scheme 0 with PPR = 42 dB was about 21, 17, and 11 dB, respectively, which are well matched within a few dB.

As shown in Figure 16, the combined CI/NCI schemes developed a dip in their initial PPR values for the cases with shorter CIs and larger J/S . This dip also appeared in the noise-only case. The PPR of stronger signal cases picked up again, but the noise-only case did not regrow as some weaker signal cases didn't. These dips are attributed to the effect of *squaring loss* (SL) during the initial short coherent integration in which noise and jamming dominated until the accumulated signal started to become meaningful (Betz & Cerruti, 2020; Esteves et al., 2016; Lowe, 1999; Rodríguez et al., 2004; Strassle et al., 2007; Woo, 2000; Yang et al., 2020a).

However, the PPR of some cases even after a larger NCI did not exceed their very initial level. In these cases, it was not the non-coherent integration of the signal but the averaging-out of noise and jamming that determined the detection performance. As such, a variable detection threshold could be set, which would decrease as a combined CI/NCI scheme progressed in order to locate the weak signals, quite counter-intuitively due to the nonlinear effect.

Roughly speaking, $J/S = 51$ dB is equivalent to $C/N_0 = 20$ dB-Hz within 10.23 MHz. Since the coherent integration only uses even chips, the effective C/N_0 was reduced by 3 dB to 17 dB-Hz. When the CI = 1,000 ms, the equivalent SNR in the 1-Hz bandwidth was 17 dB, which is the PPR of Scheme 0 at the end showed in Figure 15. For Scheme 1, the equivalent SNR in the 200-Hz bandwidth for CI = 5 ms was -6 dB, which was boosted to 5.5 dB after the NCI = 200. Due to the SL of 3 dB, the equivalent SNR was 2.5 dB while the experimental value was about 1 dB as shown in Figure 16(a).

For Scheme 2, the equivalent SNR in the 50-Hz bandwidth for CI = 20 ms was 0 dB, which was boosted to 6.5 dB after NCI = 20. After the SL of 3 dB, the equivalent SNR was about 3.5 dB, which is near the experimental value of the 3 dB shown in Figure 16(b). Finally, for Scheme 3, the equivalent SNR in the 10-Hz bandwidth for CI = 100 ms was 7 dB, which was boosted to 12 dB after the NCI = 10. Due to the squaring loss of 3 dB, the equivalent SNR was about 7 dB vs. the experimental 6.5 dB shown in Figure 16(c).

On the other hand, for low J/S cases in which the interference was comparable to the noise level, the output SNR in ratio can be written as $(s/n)_{\text{out}} = P_s/(P_n + P_j) = (P_s/P_n)/(1 + P_j/P_n) \approx (P_s/P_n)/2 = (s/n)_{\text{in}}/2$ when $P_j/P_n \approx 1$. In dB, $(S/N)_{\text{out}} \approx (S/N)_{\text{in}} - 3$. For Scheme 0, $(S/N)_{\text{in}} = 45$ dB in the 1-Hz bandwidth after the 1-s coherent integration under an open-sky condition of $C/N_0 = 45$ dB-Hz before jamming insertion. As a result, $(S/N)_{\text{out}} = 45 - 3 = 42$ dB, which matches the top first curve well at J/S = 10 dB shown in Figure 15.

Similarly for Scheme 2, the SNR in the 50-Hz bandwidth for CI = 20 ms was $45 - 17 = 28$ dB, which was boosted to 6.5 dB after NCI = 20 (no SL at high SNRs), leading to $(S/N)_{\text{in}} = 34.5$ dB, and $(S/N)_{\text{out}} = (S/N)_{\text{in}} - 3 = 34.5 - 3 = 31.5$ dB, which is close to the top first curve at J/S = 10 dB as shown in Figure 16(b). The analysis also holds for Schemes 1 and 3.

When the input J/S went from 10 dB to 51 dB, an increase of 41 dB (the first and eighth curves from the top in Figures 15 and 16), the output PPR for Scheme 0 went down from 42 dB to 17 dB, a reduction of 25 dB as shown in Figure 15. Similarly, a reduction of 9, 22, and 25 dB for Schemes 1, 2, and 3 was observed, respectively. There was no linear relationship between the change of the input J/S and that of the output PPR, but they can be accounted for by such factors as $S/(N+J)$, CI, \sqrt{NCI} , and SL, as analyzed above.

In the initial demonstration, the test data with a smaller number of frequency bins and hundred code phases were considered for a ballpark analysis. Test runs may one day be extended to cover wider time and frequency search intervals, further taking into consideration such implementation losses as quantization errors on FPGA and arithmetic rounding-off errors on ARM, among others. Theoretical analysis is of interest using the system detection and false alarm probabilities (Borio et al., 2006a) as well as extreme value theory (Gumbel, 2004; Turunen, 2007) and the advanced concepts of effective C/N_0 (Borio et al., 2006b) and spectral separation coefficients (SSC; Betz, 2000, 2001).

4.6 | Receiver Operating Characteristics (ROC)

The *receiver operating characteristics* (ROC) curve is defined as the probability of detection (P_d) as a function of the probability of false alarm (P_{fa}). In our case of signal acquisition, P_d is therefore the probability of detecting a desired signal under the H_1 hypothesis that the signal is present. P_{fa} is the probability of declaring the presence of a signal under the hypothesis H_0 in which there are only noise and interference without the signal.

A total of 400 runs, 200 for H_1 and 200 for H_0 , were made in the Monte Carlo simulation to estimate the ROC curves for the CCLCI method. A single sideband signal of BOC(10, 5) was subject to a white noise with SNR = -10 dB and an MSJ of J/S = 53 dB. The signal was sampled at $f_s = 4f_c$, $f_c = 20.46$ Msp.

The initial timing uncertainty was 10 chips, which was covered by 40 correlators and spaced by one sample for the code phase search. The initial frequency uncertainty was ± 1 kHz, which was covered by five frequency search bins with the coarse

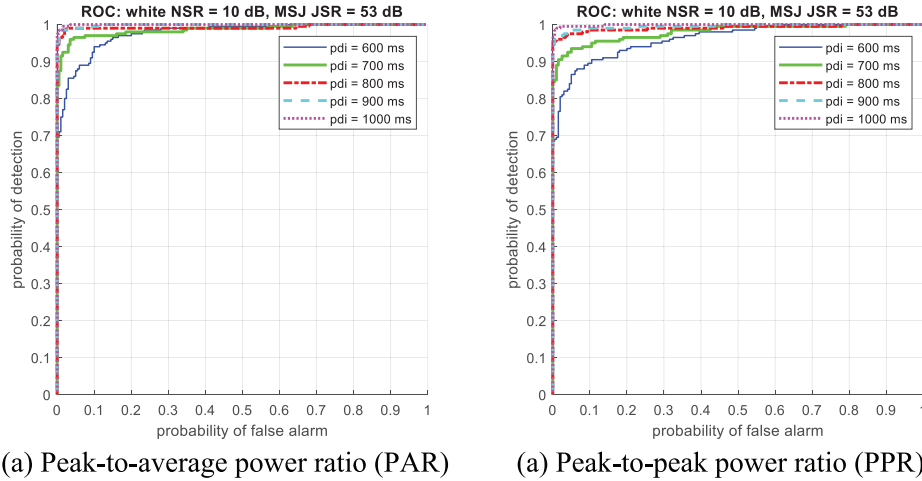


FIGURE 17 Estimated ROC curves for different PDIs under $\text{SNR} = -10$ dB and $J/S = 53$ dB from Monte Carlo simulations

frequency search spacing of 500 Hz for the short correlation interval of $T_1 = 1$ ms. The actual frequency was at $f_d = 249.75$ Hz, which is close to the largest frequency error possible of 250 Hz between two frequency search bins.

In the simulation, PDI varied from 600 ms to 1,000 ms with an increment of 100 ms as shown in Figure 17. The corresponding refined frequency search spacing was chosen to be $1/(2 \times \text{PDI})$. At PDI = 1,000 ms, the spacing was 0.5 Hz, and the residual frequency error for $f_d = 249.75$ Hz was -0.25 Hz relative to the coarse bin at 500 Hz, which represents a worst-case scenario with the largest possible frequency error.

Two test statistics were generated at the search grid points for detection: one was the correlation peak-to-noise floor average power ratio (PAR) and the other was the peak-to-noise floor peak power ratio (PPR), both excluding the mainlobe (± 2 and ± 4 in frequency and time directions, respectively) around the point under test. The comparison of the two plots in Figure 17, though simplistic, indicates that PAR outperforms PPR in terms of ROC curves, which is consistent with the observations made in Geiger et al. (2012).

In our embedded implementation shown in Figure 15, keeping the two largest peaks when stepping through frequency bins and code phases proved to be faster and easier than obtaining the average across the entire time and frequency search zone, thus is the logic behind the choice of PPR over PAR, a trade-off of performance for complexity.

4.7 | Clock Stability for Handover from Acquisition to Tracking

Local oscillator stability (or lack of it) remains an important performance-limiting factor in long coherent integration. The phase noise (short-term stability) effectively has two effects on correlation, namely, the expected correlation peak decreases and the peak variance increases with noise (Serna et al., 2010). Due to the de-coherence of the carrier, the signal energy accumulation no longer increases linearly with time, limiting the ultimate sensitivity level one can expect from long coherent integration (Watson et al., 2006). As an example, the saturation of partial sums as

shown in Figure 10(b) is attributed to the combined effect of uncompensated frequency error and clock instability that manifests in long integration.

In Dominguez et al. (2016), three types of clocks, namely, TCXO ($h_0 = 9.43 \times 10^{-20}$, $h_{-2} = 3.8 \times 10^{-21}$), CSAC ($h_0 = 7.2 \times 10^{-21}$, $h_{-2} = 2.7 \times 10^{-27}$), and OCXO ($h_0 = 3.4 \times 10^{-22}$, $h_{-2} = 1.3 \times 10^{-24}$), were analyzed for their effects on coherent integration. TCXO could be used to integrate up to 100 ms coherently but not satisfactorily when the coherent integration time is 500 ms and beyond. CSAC could be used for coherent integration up to 500 ms, but shows considerable degradation at 1,000 ms. In contrast, OCXO could integrate coherently up to 1,000 ms with inconsequential effects from the phase noise.

For the embedded implementation described in the previous section, the samples of the incoming signal over 1 second were stored in a double data rate (DDR) memory and repeatedly processed faster than real-time for searching through the time-frequency uncertainty zone, which would have otherwise taken hundreds of seconds to find the first satellite. Once detected, an estimate of the elapsed time from the start of data collection was then propagated forward to the live signal. Clearly, a concern arises about the long-term stability on the order of several hundred seconds; that is, the oscillator drift over the search period may cause *time deviation* (TDEV) of an appreciable size with respect to the correlator acquisition window.

If the return from playback to live samples misses the signal (i.e., cannot find it where it was predicted), one has to search around that spot anew, albeit with a much-reduced uncertainty. TDEV can thus be expressed in terms of the modified Allan deviation as $TDEV \approx \tau \sigma_y(\tau)$ where τ is the observation time. As an example, a Biley LP62 OXCO has a TDEV on the order of 10^{-9} s for $\tau \sim 100$ s. With 1,024 correlators spaced at 0.454 chips at 5.115 MHz, the acquisition window amounts to 9.1×10^{-5} s. For this case, the 3-sigma timing propagation error remains well within the acquisition window. In general, the goal of the system design (the tolerance that can be accommodated) was to ensure that the three-sigma predicted interval would be well within the parallel correlators so that the code and carrier tracking loops could be closed once a signal is acquired.

5. | CONCLUSION

In this paper, we presented a two-stage method for standalone direct acquisition of multi-band split-spectrum binary offset modulation (BOC) signals via coherent combining and long coherent integration (CCLCI), useful when the incoming signal is weak and/or when the radio-frequency interference (RFI) is strong. The proposed method extracts individual sidebands of a split-spectrum signal and processes them separately. As such, it avoids the multiple peak ambiguity but needs to combine the individual sideband correlations to recover the reduced strength due to spectrum splitting. Similar combining is also needed for signals in different frequency bands.

To carry out the long coherent integration, the first stage applies short-term correlations for coarse frequency search, followed by a second stage with refined frequency search. CCLCI maximizes the overall gain by applying phase rotation, code migration correction, and frequency divergence compensation in long coherent integration as well as time and frequency adjustment in the combination of data-modulated and data-less components, upper and lower sidebands, and signals on different frequencies. Prototyping of the design with a software-defined radio (SDR) receiver on an FPGA/ARM platform was evaluated in an embedded

demonstration in which the algorithm was validated with RF signals generated from a Spirent GPS RF Simulator. The sample results presented in this paper clearly illustrate the functionality and performance of CCLCI.

The method in present form is attractive for signals with a pilot component (either time-multiplexed or orthogonal-modulated) or signals with data of a slow symbol rate. The challenges remain for signals with faster symbol rates and/or the presence of fast secondary codes (e.g., 1 kHz) especially in standalone receivers. In a cluttered environment, multipath is omnipresent. The presence of close-in multipath components has the effect of enlarging the correlation function width and raising its main peak if constructive. Both are, in fact, favorable for discrete acquisition searches in the code phase space. Furthermore, long coherent integration with a refined frequency resolution (e.g., 0.5 Hz) helps isolate/mitigate individual multipath components. However, severe fading (i.e., a destructive sum of multipath components of comparable amplitude but in an opposite phase) does occur instantaneously, which results in a loss of accumulated signal energy.

Signal propagation (through ionosphere) and receiver antenna/RF impairments introduce an uneven distortion across the signal bandwidth. The difference in group delay between the upper and lower sidebands when the sideband separation is large and between signals at different frequency bands (e.g., L1 and L2) becomes an important factor to consider for coherent combining, which entails an additional search in the delay space, a trade-off between performance gain and implementation complexity.

Another limiting factor is clock stability. Short-term stability with low phase noise is desired for long coherent integration in seconds, whereas long-term stability on the order of hundreds of seconds in our application is required to ensure seamless handover from acquisition to tracking. Efforts are underway for a complete implementation with handover to tracking, more rigorous assessment of the achievable performance, and high-sensitivity GNSS receiver applications.

ACKNOWLEDGMENTS

This research was supported in part under Air Force SBIR Contract No. FA8650-18-C-1145, which is gratefully acknowledged. Thanks also go to Mat Cosgrove, Taylor Schluter, Bo Halamandaris, and Jeff Dickman of Northrop Grumman Systems Corporation (Woodland Hills, CA) for their efforts in embedded implementation and demonstrations. Approved for public release, CLEARED on May 22, 2020 (Case Number 88ABW-2020-1838). US patent pending (63/204,805).

REFERENCES

- Akopian, D. (2001). A fast satellite acquisition method. *Proc. of the 14th International Technical Meeting of the Satellite Division of the Institute of Navigation (ION GPS 2001)*, Salt Lake City, UT, 2871–2881. <https://www.ion.org/publications/abstract.cfm?articleID=1963>
- Barker, B. C., Betz, J. W., Clark, J. E., Correia, J. T., Gillis, J. T., Lazar, S., Rehorn, K. A., & Straton, J. R. (2000). Overview of the GPS M code signal. *Proc. of the 2000 National Technical Meeting of the Institute of Navigation*, Anaheim, CA, 542–549. <https://www.ion.org/publications/abstract.cfm?articleID=66>
- Betz, J. W. (1984). Performance of the deskewed short-time correlator. *IEEE International Conference on Acoustics, Speech, and Signal Processing (ICASSP '84)*, San Diego, CA, 628–631. <https://doi.org/10.1109/ICASSP.1984.1172294>
- Betz, J. W. (1999). The offset carrier modulation for GPS modernization. *Proc. of the 1999 National Technical Meeting of the Institute of Navigation*, San Diego, CA, 639–648. <https://www.ion.org/publications/abstract.cfm?articleID=716>
- Betz, J. W. (2000). Effect of narrowband interference on GPS code tracking accuracy. *Proc. of the 2000 National Technical Meeting of the Institute of Navigation*, Anaheim, CA, 16–27. <https://www.ion.org/publications/abstract.cfm?articleID=3>

- Betz, J. W. (2001). Effect of partial-band interference on receiver estimation of C/N_0 : Theory. *Proc. of the 2001 National Technical Meeting of the Institute of Navigation*, Long Beach, CA, 817–828. <https://www.ion.org/publications/abstract.cfm?articleID=195>
- Betz, J. W. (2015). *Engineering satellite-based navigation and timing: Global navigation satellite systems, signals, and receivers*. Wiley-IEEE Press.
- Betz, J. W., Capozza, P., & Fite, J. (2002). System for direct acquisition of received signals (U.S. Patent No. 7,224,721). U.S. Patent and Trademark Office. <https://patents.justia.com/patent/7224721>
- Betz, J. W., Capozza, P., & Fite, J. (2007). System for direct acquisition of received signals (U.S. Patent No. 7,447,259). U.S. Patent and Trademark Office. <https://patents.justia.com/patent/7447259>
- Betz, J. W., & Cerruti, A. P. (2020). Performance of dual-channel codeless and semicodeless processing. *NAVIGATION*, 67(1), 109–128. <https://doi.org/10.1002/navi.347>
- Betz, J. W., Fite, J. D., & Capozza, P. T. (2004). DirAc: An integrated circuit for direct acquisition of the M-code signal. *Proc. of the 17th International Technical Meeting of the Satellite Division of the Institute of Navigation (ION GNSS 2004)*, Long Beach, CA, 447–456. <https://www.ion.org/publications/abstract.cfm?articleID=5677>
- Borio, D. (2008). FFT sign search with secondary code constraints for GNSS signal acquisition. *2008 IEEE 68th Vehicular Technology Conference*, Calgary, AB. <https://doi.org/10.1109/VETECF.2008.142>
- Borio, D., Camoriano, L., & Presti, L. L. (2006a). Impact of acquisition searching strategy on the detection and false alarm probabilities in a CDMA receiver. *2006 IEEE/ION Position, Location, And Navigation Symposium*, Coronado, CA, 1100–1107. <https://doi.org/10.1109/PLANS.2006.1650716>
- Borio, D., O'Driscoll, C., & Lachapelle, G. (2009). Coherent, noncoherent, and differentially coherent combining techniques for acquisition of new composite GNSS signals. *IEEE Transactions on Aerospace and Electronic Systems*, 45(3), 1227–1240. <https://doi.org/10.1109/TAES.2009.5259196>
- Borio, D., Presti, L. L., & Mulassano, P. (2006b). Spectral separation coefficients for digital GNSS receivers. *2006 14th European Signal Processing Conference*, Florence, Italy. <https://ieeexplore.ieee.org/document/7071499>
- Burian, A., Lohan, E. S., & Renfors, M. (2006). BPSK-like methods for hybrid-search acquisition of Galileo signals. *2006 IEEE International Conference on Communications*, Istanbul, Turkey. <https://doi.org/10.1109/ICC.2006.255493>
- Corazza, G. E., & Pedone, R. (2007). Generalized and average likelihood ratio testing for post detection integration. *IEEE Transactions on Communications*, 55(11), 2159–2171. <https://doi.org/10.1109/TCOMM.2007.908531>
- Dafesh, P., Holmes, J. K., Cahn, C. R., & Stansell, T. (2002). Description and analysis of time-multiplexed M-code data. *Proc. of the 58th Annual Meeting of the Institute of Navigation and CIGTF 21st Guidance Test Symposium*, Albuquerque, NM, 598–611. <https://www.ion.org/publications/abstract.cfm?articleID=991>
- Deambrogio, L., Bastia, F., Palestini, C., Pedone, R., Villanti, M., & Corazza, G. E. (2013). Cross-band aided code acquisition in dual-band GNSS receivers. *IEEE Transactions on Aerospace and Electronic Systems*, 49(4), 2533–2545. <https://doi.org/10.1109/TAES.2013.6621834>
- Dominguez, E., Pousinho, A., Boto, P., Gómez-Casco, D., Locubiche-Serra, S., Seco-Granados, G., López-Salcedo, J. A., Fragner, H., Zangerl, F., Peña, O., & Jiménez-Baños, D. (2016). Performance evaluation of high sensitivity GNSS techniques in indoor, urban, and space environments. *Proc. of the 29th International Technical Meeting of the Satellite Division of the Institute of Navigation (ION GNSS+ 2016)*, Portland, OR, 373–393. <https://doi.org/10.33012/2016.14677>
- Dovis, F. & Ta, T. H. (2012). High sensitivity techniques for GNSS signal acquisition. In S. Jin (Ed.), *Global navigation satellite systems: Signal, theory and applications* (pp. 3–30). InTech. <https://www.doi.org/10.5772/29453>
- Esteves, P., Sahnoudi, M., & Boucheret, M.-L. (2016). Sensitivity characterization of differential detectors for acquisition of weak GNSS signals. *IEEE Transactions on Aerospace and Electronic Systems*, 52(1), 20–37. <https://doi.org/10.1109/TAES.2015.130470>
- Fine, P. & Wilson, W. (1999). Tracking algorithm for GPS offset carrier signals. *Proc. of the 1999 National Technical Meeting of the Institute of Navigation*, San Diego, CA, 671–676. <https://www.ion.org/publications/abstract.cfm?articleID=719>
- Fishman, P. M. & Betz, J. W. (2000). Predicting performance of direct acquisition for the M-code signal. *Proc. of the 2000 National Technical Meeting of the Institute of Navigation*, Anaheim, CA, 574–582. <https://www.ion.org/publications/abstract.cfm?articleID=68>
- Foucras, M., Julien, O., Macabiau, C., & Ekambi, B. (2014). Detailed analysis of the impact of the code Doppler on the acquisition performance of new GNSS signals. *Proc. of the 2014 International Technical Meeting of the Institute of Navigation*, San Diego, CA, 513–524. <https://www.ion.org/publications/abstract.cfm?articleID=11520>
- Geiger, B. C., Vogel, C., & Soudan, M. (2012). Comparison between ratio detection and threshold comparison for GNSS acquisition. *IEEE Transactions on Aerospace and Electronic Systems*, 48(2), 1772–1779. <https://doi.org/10.1109/TAES.2012.6178098>

- Gómez-Casco, D., López-Salcedo, J. A., & Seco-Granados, G. (2020). Optimal post-detection integration techniques for the reacquisition of weak GNSS signals. *IEEE Transactions on Aerospace and Electronic Systems*, 56(3), 2302–2311. <https://doi.org/10.1109/TAES.2019.2948449>
- Gumbel, E. J. (2004). *Statistics of extremes*. Dover Publications.
- Gunawardena, S. (2007). *Development of a transform-domain instrumentation global positioning system receiver for signal quality and anomalous event monitoring* [Doctoral dissertation, Ohio University]. http://rave.ohiolink.edu/etdc/view?acc_num=ohiou1178558967
- Guo, Y., Huan, H., Tao, R., & Wang, Y. (2017). Long-term integration based on two-stage differential acquisition for weak direct sequence spread spectrum signal. *IET Communications*, 11(6), 878–886. <https://doi.org/10.1049/iet-com.2016.0996>
- Gusi, A., Closas, P., & Garcia-Molina, J. A. (2016). False lock probability in BOC signals. *Proc. of the 2016 International Technical Meeting of the Institute of Navigation*, Monterey, CA, 618–623. <https://doi.org/10.33012/2016.13440>
- Hao, F., Yu, B., Gan, X., Jia, R., Zhang, H., Huang, L., & Wang, B. (2020). Unambiguous acquisition/tracking technique based on sub-correlation functions for GNSS sine-BOC signals. *Sensors*, 20(2). <https://doi.org/10.3390/s20020485>
- Heiries, V., Roviras, D., Ries, L., & Calmettes, V. (2004). Analysis of non-ambiguous BOC signal acquisition performance. *Proc. of the 17th International Technical Meeting of the Satellite Division of the Institute of Navigation (ION GNSS 2004)*, Long Beach, CA, 2611–2622. <https://www.ion.org/publications/abstract.cfm?articleID=5945>
- Hodgart, M. S. & Simons, E. (2012). Improvements and additions to the double estimation technique. *2012 6th ESA Workshop on Satellite Navigation Technologies (Navitec 2012) & European Workshop on GNSS Signals and Signal Processing*, Noordwijk, Netherlands. <https://doi.org/10.1109/NAVITEC.2012.6423053>
- Holmes, J. K., Raghavan, S., Dafesh, P., & Lazar, S. (1999). Effective signal to noise ratio performance comparison of some GPS modernization signals. *Proc. of the 12th International Technical Meeting of the Satellite Division of the Institute of Navigation (ION GPS 1999)*, Nashville, TN, 1755–1762. <https://www.ion.org/publications/abstract.cfm?articleID=3329>
- Jiao, X., Wang, J., & Li, X. (2012). High sensitivity GPS acquisition algorithm based on code Doppler compensation. *2012 IEEE 11th International Conference on Signal Processing*, Beijing, China. <https://doi.org/10.1109/ICoSP.2012.6491645>
- Jiménez-Baños, D., Blanco-Delgado, N., López-Risueño, G., Seco-Granados, G., & Garcia-Rodríguez, A. (2006). Innovative techniques for GPS indoor positioning using a snapshot receiver. *Proc. of the 19th International Technical Meeting of the Satellite Division of the Institute of Navigation (ION GNSS 2006)*, Fort Worth, TX, 2944–2955. <https://www.ion.org/publications/abstract.cfm?articleID=6834>
- Julien, O., Macabiau, C., Cannon, M. E., & Lachapelle, G. (2007). ASPeCT: Unambiguous sine-BOC(n, n) acquisition/tracking technique for navigation applications. *IEEE Transactions on Aerospace and Electronic Systems*, 43(1), 150–162. <https://doi.org/10.1109/TAES.2007.357123>
- Kong, S.-H. (2015). SDHT for fast detection of weak GNSS signals. *IEEE Journal on Selected Areas in Communications*, 33(11), 2366–2378. <https://doi.org/10.1109/JSAC.2015.2430291>
- Kong, S.-H. (2017). High Sensitivity and fast acquisition signal processing techniques for GNSS receivers: From fundamentals to state-of-the-art GNSS acquisition technologies. *IEEE Signal Processing Magazine*, 34(5) 59–71. <https://doi.org/10.1109/MSP.2017.2714201>
- Krasner, N. F. (1997). *GPS receiver and method for processing GPS signals*, (U.S. Patent No. 5,781,156). U.S. Patent and Trademark Office. <https://patents.justia.com/patent/5781156>
- Leclère, J., Botteron, C., & Farine, P.-A. (2017). High sensitivity acquisition of GNSS signals with secondary code on FPGAs. *IEEE Aerospace and Electronic Systems Magazine*, 32(8), 46–63. <https://doi.org/10.1109/MAES.2017.160176>
- Leclère, J., Landy, R. J. R., & Botteron, C. (2016). How does one compute the noise power to simulate real and complex GNSS signals? *InsideGNSS*, 29–33. <https://insidengss.com/how-does-one-compute-the-noise-power-to-simulate-real-and-complex-gnss-signals/>
- Li, Y., Zeng, T., Long, T., & Wang, Z. (2006). Range migration compensation and Doppler ambiguity resolution by Keystone transform. *2006 CIE International Conference on Radar*, Shanghai, China. <https://doi.org/10.1109/ICR.2006.343404>
- Lowe, S. T. (1999). *Voltage signal-to-noise ratio (SNR) nonlinearity resulting from incoherent summations* (Report TMO PR-42-137). The Telecommunications and Mission Operations. [https://www.semanticscholar.org/paper/Voltage-Signal-to-Noise-Ratio-\(SNR\)-Nonlinearity-Lowe/58cce9808fc75ed307c676613f2ba9efabd4bf67](https://www.semanticscholar.org/paper/Voltage-Signal-to-Noise-Ratio-(SNR)-Nonlinearity-Lowe/58cce9808fc75ed307c676613f2ba9efabd4bf67)
- O'Driscoll, C. & Curran, J. T. (2016). Codeless code tracking of BOC signals. *Proc. of the 29th International Technical Meeting of the Satellite Division of the Institute of Navigation (ION GNSS+ 2016)*, Portland, OR, 497–508. <https://doi.org/10.33012/2016.14842>
- Pany, T. (2010). *Voltage signal processing for GNSS software receivers*, Artech House. <https://us.artechhouse.com/Navigation-Signal-Processing-for-GNSS-Software-Receivers-P1325.aspx>
- Pany, T. (2020). *Private communications*.
- Pany, T., Riedl, B., Winkel, J., Woerz, T., Schweikert, R., Niedermeier, H., Lagrasta, S., Lopez-Risueño, G., & Jiménez-Banos, D. (2009). Coherent integration time: The longer the better.

- InsideGNSS*, 52–61. https://www.researchgate.net/publication/308355946_Coherent_integration_time_The_longer_the_better
- Psiaki, M. L. (2001). Block acquisition of weak GPS signals in a software receiver. *Proc. of the 14th International Technical Meeting of the Satellite Division of the Institute of Navigation (ION GPS 2001)*, Salt Lake City, UT, 2838–2850. <https://www.ion.org/publications/abstract.cfm?articleID=1960>
- Rodríguez, J. Á. Á, Pany, T., & Eissfeller, B. (2004). Theory of acquisition algorithms for indoor positioning. *2nd ESA Workshop on Satellite Navigation User Equipment Technologies (NAVITEC'2004)*, Noordwijk, Netherlands. https://www.researchgate.net/publication/228855044_Theory_on_Acquisition_algorithms_for_indoor_positioning
- Rushanan, J. J. & Winters, D. W. (2010). Modeling distributions of non-coherent integration sidelobes. *Proc. of the 2010 International Technical Meeting of the Institute of Navigation*, San Diego, CA, 895–908. <https://www.ion.org/publications/abstract.cfm?articleID=8870>
- Seco-Granados, G., López-Salcedo, J., Jiménez-Baños, D., & López-Risueño, G. (2012). Challenges in indoor global navigation satellite systems: Unveiling its core features in signal processing. *IEEE Signal Processing Magazine*, 29(2), 108–131. <https://doi.org/10.1109/MSP.2011.943410>
- Serna, E. P., Thombre, S., Valkama, M., Lohan, S., Syrjälä, V., Hurskainen, H., & Nurmi, J. (2010). Local oscillator phase noise effects on GNSS code tracking. *InsideGNSS*, 52–62. <https://www.insidegnss.com/auto/novdec10-Thombre.pdf>
- Soloviev, A. & Dickman, J. (2011). Extending GPS carrier phase availability indoors with a deeply integrated receiver architecture. *IEEE Wireless Communications*, 18(2), 36–44. <https://doi.org/10.1109/MWC.2011.5751294>
- Soloviev, A. & Dickman, J. (2014). Collaborative signal processing. *GPS World*. <https://www.gpsworld.com/collaborative-signal-processing/>
- Soloviev, A., Gunawardena, S., & van Graas, F. (2008). Deeply integrated GPS/low-cost IMU for low CNR signal processing: Concept description and in-flight demonstration. *NAVIGATION*, 55(1), 1–13. <https://www.ion.org/publications/abstract.cfm?articleID=102458>
- Soloviev, A., Toth, C., & Grejner-Brzezinska, D. (2012). Performance of deeply integrated GPS/INS in dense forestry areas. *Journal of Applied Geodesy*, 6(1). <https://doi.org/10.1515/jag-2011-0005>
- Strassle, C., Megnet, D., Mathis, H., & Burgi, C. (2007). The squaring-loss paradox. *Proc. of the 20th International Technical Meeting of the Satellite Division of the Institute of Navigation (ION GNSS 2007)*, Fort Worth, TX, 2715–2722. <https://www.ion.org/publications/abstract.cfm?articleID=7534>
- Seppo, T. (2005). Combinatorial loss in satellite acquisition. *Proc. of the 18th International Technical Meeting of the Satellite Division of the Institute of Navigation (ION GNSS 2005)*, Long Beach, CA, 890–895. <https://www.ion.org/publications/abstract.cfm?articleID=6283>
- Svaton, J. & Vejražka, F. (2020). Joint acquisition estimator of modern GNSS tiered signals using block pre-correlation processing of secondary code. *Sensors*, 20(10), 2965. <https://doi.org/10.3390/s20102965>
- Turunen, S. (2007). Network assistance: What will new GNSS signals bring to it? *InsideGNSS*, 35–41. https://www.insidegnss.com/auto/igm_035-041.pdf
- Watson, R., Lachapelle, G., & Klukas, R. (2006). Testing oscillator stability as a limiting factor in extreme high-sensitivity GPS applications. *Proc. of the European Navigation Conference 2006*, Manchester, UK. https://www.researchgate.net/publication/229035625_Testing_oscillator_stability_as_a_limiting_factor_in_extreme_high-sensitivity_GPS_applications
- Ward, P. W. (2003a). A design technique to remove the correlation ambiguity in binary offset carrier (BOC) spread spectrum signals. *Proc. of the 59th Annual Meeting of the Institute of Navigation and CIGTF 22nd Guidance Test Symposium*, Albuquerque, NM, 146–155. <https://www.ion.org/publications/abstract.cfm?articleID=3844>
- Ward, P. W. (2003b). M code performance spreadsheet analysis techniques. *Proc. of the 16th International Technical Meeting of the Satellite Division of the Institute of Navigation (ION GPS/GNSS 2003)*, Portland, OR, 1553–1560. <https://www.ion.org/publications/abstract.cfm?articleID=5340>
- Woo, K. T. (2000). Optimum semicodeless carrier-phase tracking of L2. *NAVIGATION*, 47(2), 82–99. <https://doi.org/10.1002/j.2161-4296.2000.tb00204.x>
- Wu, C., Xu, L.-P., Zhang, H., & Zhao, W.-B. (2015). A block zero-padding method based on DCFT for L1 parameter estimations in weak signal and high dynamic environments. *Frontiers of Information Technology & Electronic Engineering*, 16, 796–804. <https://doi.org/10.1631/FITEE.1500058>
- Yang, C. & Han, S. (2006). Block-accumulating coherent integration over extended interval (BACIX) for weak GPS signal acquisition. *Proc. of the 19th International Technical Meeting of the Satellite Division of the Institute of Navigation (ION GNSS 2006)*, Fort Worth, TX, 2427–2440. <https://www.ion.org/publications/abstract.cfm?articleID=6820>
- Yang, C. & Han, S. (2007). Tracking of weak GPS signal with BACIX. *Proc. of the 20th International Technical Meeting of the Satellite Division of the Institute of Navigation (ION GNSS 2007)*, Fort Worth, TX, 2797–2807. <https://www.ion.org/publications/abstract.cfm?articleID=7543>

- Yang, C. & Soloviev, A. (2016). Joint acquisition of GNSS codes via coherent combining of multi-frequency composite quadrature signals. *Proc. of the 2016 International Technical Meeting of the Institute of Navigation*, Monterey, CA, 805–819. <https://doi.org/10.33012/2016.13489>
- Yang, C., Soloviev, A., & Ha, J. C. (2019). Standalone direct acquisition of weak multi-band split-spectrum signals. *Proc. of the 32nd International Technical Meeting of the Satellite Division of the Institute of Navigation (ION GNSS+ 2019)*, Miami, FL, 3997–4010. <https://doi.org/10.33012/2019.17111>
- Yang, C., Soloviev, A., & Ha, J. C. (2020a). Combining and integration schemes for acquisition of weak GNSS split-spectrum signals. *Proc. of the 2020 International Technical Meeting of the Institute of Navigation*, San Diego, CA, 713–725. <https://doi.org/10.33012/2020.17172>
- Yang, C., Soloviev, A., Vadlamani, A., & Ha, J. C. (2020b). Long coherent combining and integration for BOC signal acquisition under strong interference. *Proc. of the 33rd International Technical Meeting of the Satellite Division of the Institute of Navigation (ION GNSS+ 2020)*, 2758–2778. <https://doi.org/10.33012/2020.17593>
- Yao, Z. (2012). Unambiguous processing techniques of binary offset carrier modulated signals. In S. Jin (Ed.), *Global navigation satellite systems: Signal, theory, and applications*. <https://www.doi.org/10.5772/30649>
- Ziedan, N. I. (2006). *GNSS receivers for weak signals*. Artech House. <https://us.artechhouse.com/GNSS-Receivers-for-Weak-Signals-P969.aspx>

How to cite this article: Yang, C., Soloviev, A., Vadlamani, A., & Ha, J. (2022) Coherent combining and long coherent integration for BOC signal acquisition under strong interference. *NAVIGATION*, 69(1). <https://doi.org/10.33012/navi.508>